Applied Catalysis B: Environmental 310 (2022) 121319

Contents lists available at ScienceDirect

Applied Catalysis B: Environmental

journal homepage: www.elsevier.com/locate/apcatb

Surface-layer bromine doping enhanced generation of surface oxygen vacancies in bismuth molybdate for efficient photocatalytic nitrogen fixation

Guoan Wang, Tingting Huo, Quanhua Deng, Fei Yu, Yuguo Xia, Haiping Li *, Wanguo Hou

National Engineering Research Center for Colloidal Materials, School of Chemistry and Chemical Engineering, Shandong University, Jinan, Shandong 250100, China

A R T I C L E I N F O

Keywords:
Bismuth molybdate
Photocatalysis
Nitrogen fixation
Br doping
Oxygen vacancy

A B S T R A C T

The oxygen vacancy (Ov) in photocatalysts plays a significant role for N_2 fixation, but effective and simple means for creation of Ov are in urgent demand. Herein, surface-layer Br doping was confirmed to create massive surface Ov in Bi_2MoO_6 in a solvothermal process, with the product (BMO-Br-Ov) exhibiting remarkably enhanced N_2 chemisorption and activation, photoinduced charge separation, and thus photocatalytic N_2 fixation, compared with bulk Bi_2MoO_6, with an apparent quantum yield at 420 nm reaching 0.52% in pure water and 2.56% in the methanol aqueous solution. The charge separation enhancement benefits from the Ov introduced defect level and Br doping and surface Ov modification induced band-level difference between the surface and the inside in BMO-Br-Ov that leads to fabrication of the surface/inside homojunction. This work provides a simple way to create surface Ov in Bi_2MoO_6 and may direct Ov creation in other Bi-based photocatalysts for efficient N_2 fixation.

1. Introduction

Ammonia (NH_3), extensively used as a key component in industrial synthesis of many chemicals (e.g., fertilizers), is of considerable significance to the global economic development [1]. Owing to the low efficiency of NH_3 production from plants, artificial nitrogen fixation approaches have been developed since the 19th century [2]. Nowadays, the industrial NH_3 synthesis depends on the Haber-Bosch method, i.e., producing NH_3 via the reaction of N_2 and H_2 at high temperature (300–550 °C) and pressure (100–200 atmosphere) with the strong N≡N bond (~941 kJ mol^{-1}) dissociated, [3] which accounts for ~1–2% of annual energy consumption and ~1% of the annual CO_2 emission of the world [4]. In recent years, photocatalytic nitrogen fixation that allows direct production of NH_3 from N_2 and H_2O attracts great interest of scientists owing to its advantages in energy and environment, [5,6] but the photocatalytic efficiency is still low and mainly restricted by two factors including N_2 adsorption and activation and the difficulty for photocatalysts to supply six electrons to reduce one N_2 molecule [7].

Bismuth-based compounds have been widely researched on photocatalytic nitrogen fixation because of their appropriate energy band levels (e.g., hybridization of Bi 6 s and O 2p orbits to shallow the valence bands and narrow the bandgaps), high chemical stability, low toxicity and cost [8,9], and especially easy creation of defects (mainly oxygen vacancies (simply marked as Ov)) [2]. As is known, vacancies and heteroatom doping play key roles in photocatalytic nitrogen reduction and the vacancies exhibits higher efficacy than the heteroatom doping in the initial N_2 adsorption and activation process that is generally the rate-determination step of N_2 reduction to NH_3 [10]. Reported Bi-based compounds include BiOX (X = Cl, Br, or I), Bi-rich BiO_xX_y (X = Br or I), $Bi_2O_2CO_3$, Bi_2O_3, and Bi_2MO_6 (M = Mo or W) [2]. In comparison, Bi_2MoO_6, as a layered Aurivillius oxide and promising visible-light-responsive photocatalyst for practical application, has been relatively little researched in photocatalytic nitrogen fixation, and related structure modification and deep mechanism insight deserve to be conducted.

Bulk Bi_2MoO_6 exhibits low photocatalytic activity in nitrogen reduction, but Fe doping [11], construction of special architectures [12], fabrication of heterojunctions [13–15] and composites [16], and creation of Ov [17,18] could effectively enhance the photoactivity of Bi_2MoO_6. Comparatively, the creation of Ov exhibits a higher potency. For instance, Li and coauthors created rich Ov in Bi_2MoO_6 via a simple and cost-effective NaOH-etching treatment process and increased the NH_3 production rate to ~40 µmol h^{-1} [18]. Hao et al. prepared Ov-containing Bi_2MoO_6 nanoframe that exhibits efficient solar-driven

* Corresponding author.
E-mail address: hpli@sdu.edu.cn (H. Li).

https://doi.org/10.1016/j.apcatb.2022.121319
Received 25 November 2021; Received in revised form 1 March 2022; Accepted 13 March 2022
Available online 16 March 2022
0926-3373/© 2022 Elsevier B.V. All rights reserved.

nitrogen fixation from air (~65 μmol h^{-1}) in absence of scavengers [17]. Beside these two methods for Ov creation in Bi_2MoO_6, there are also means including electrochemical reduction [19], $NaBH_4$ reduction [20], and common ethylene glycol-assisted solvothermal synthesis [21]. Because of crystal anisotropy of Bi_2MoO_6, i.e., atomic distribution difference in different exposed facets, chemical environment and density of Ov generated by different ways are usually different (resulting from different architectures of particles). For example, wang and coauthors reported that Br^- increases Ov on (001) facets of Bi_2MoO_6, but hardly influences that on (010) facets [22]. Therefore, it is essential to explore novel methods to synthesize Bi_2MoO_6 containing different Ov structures to further enhance the photoactivity in nitrogen fixation. According to our best knowledge, ion doping has not been used to tune Ov content in Bi_2MoO_6, though as a feasible way to create Ov in $W_{18}O_{49}$ and TiO_2 [23]. Clarifying the ion doping structure and Ov creation mechanism will largely favor the synthesis of efficient Bi_2MoO_6-based photocatalysts. In addition, the Ov in Bi_2MoO_6 was reported to enhance the photocatalytic nitrogen reduction mainly by enhancing the nitrogen chemisorption and activation [17,18], but its influence on the energy band structure, especially the defect level was rarely discussed.

In this work, surface-layer Br-doped and surface Ov-rich Bi_2MoO_6 (BMO-Br-Ov) microspheres were simply synthesized via a solvothermal process and the surface-layer Br doping remarkably enhanced the Ov formation. Relative to the bulk Bi_2MoO_6 (BMO), BMO-Br-Ov exhibits prominently enhanced photocatalytic nitrogen fixation activity, benefiting from the increased surface Ov content that leads to enhancement of photogenerated charge separation and N_2 adsorption. This work illustrates the mechanism for ion doping induced Ov formation in BMO-Br-Ov.

2. Experimental section

2.1. Synthesis of BMO and BMO-Br-Ov

BMO was synthesized by a common method. Simply, $Bi(NO_3)_3.5H_2O$ (2 mmol, 99.99%, Aladdin) and $Na_2MoO_4.2\ H_2O$ (1 mmol, 99.95%, Aladdin) were dissolved in ethylene glycol (30 mL, 99.8%, Aladdin) by sonification, respectively, and then the Na_2MoO_4 solution was slowly dropped into the $Bi(NO_3)_3$ solution under magnetic stirring. After stirring for 5 min, the resultant transparent solution was transferred into an 80-mL Teflon-lined autoclave, heated at 160 °C for 12 h, and then cooled naturally to room temperature. The final product was obtained after filtration, washing with water and ethanol several times, and dried at 60 °C for 12 h. For synthesis of BMO-Br-Ov, the $Na_2MoO_4.2H_2O$ (1 mmol) was replaced with the mixture of $KBrO_3$ (x μmol, 99.8%, Aladdin) and $Na_2MoO_4.2H_2O$ ((1000 – 0.5x) μmol) (x = 60, 80, or 100), and the product was marked as BMOx. BiOBr was prepared by substituting $KBrO_3$ (2 mmol) for $Na_2MoO_4.2H_2O$ (1 mmol). BMO-H_2O was synthesized similarly as BMO by substituting H_2O for ethylene glycol.

2.2. Characterizations

X-ray diffraction (XRD) tests were performed on an in-situ X-ray diffractometer (Rigaku SmartLab 9KW, Japan) with Cu-Kα radiation. Morphological observation was carried out by transmission electron microscopy (TEM, Jeol JEM-1011, Japan) and field emission-scanning electron microscopy (SEM, Hitachi SU8010, Japan). High-resolution TEM (HRTEM) and selected-area electron diffraction (SAED) were performed on the JEOL JEM-2100F microscope (Japan). Energy dispersive spectroscopy (EDS) was conducted on the SEM instrument. Content of C, H, and N in samples was tested by elemental analysis (Elementar Vario EL III, Germany) and metal ion content was measured by inductively coupled plasma-optical emission spectroscopy (ICP-OES, Agilent 5110, USA). X-ray photoelectron spectroscopy (XPS) was carried out on a Thermo Fisher ESCALAB 250XI spectrometer (USA). Peak positions were calibrated based on the C 1 s peak at 284.6 eV. Ultraviolet photoelectron spectroscopy (UPS) was performed on an instrument (Thermo Fisher ESCALAB XI+) with He I (21.22 eV) as the excitation source at an applied bias voltage of − 10 eV. Nitrogen adsorption-desorption isotherms were measured on a Quadrasorb EVO analyzer (Quantachrome Instruments, USA), with degassing temperature of 120 °C and time of 6 h. UV–vis diffuse reflectance spectroscopy (DRS) was conducted on a U4100 UV Spectrometer (Hitachi, Japan). Electron paramagnetic resonance (EPR) spectroscopy was carried on an A300–10/12 spectrometer (Bruker, Germany) at room temperature (microwave frequency, 9.85 GHz; center field, 3510 G; sweep width, 100 G; modulation frequency, 100 kHz; and modulation amplitude, 1.00 G), in the dark or under visible light irradiation from a 300-W Xe lamp (CEL-HXF300, Ceaulight, China) equipped with a cutoff filter ($\lambda \geq$ 420 nm). The temperature-programmed desorption (TPD) of N_2 on samples was tested on an AutoChem1 II 2920 chemisorption analyzer (USA). In-situ Fourier transform infrared spectroscopy (FT-IR) was performed on a TENSOR II FT-IR spectrometer (Bruker, Germany). Thermogravimetric (TG) and differential scanning calorimetry (DSC) analysis were conducted on a synchronous thermal analyzer (Netzsch STA449C Jupiter, Germany). Photoluminescence (PL) spectroscopy was carried out on a FluoroMax-4 spectrophotometer (Horiba, Japan) at room temperature, with excitation and emission slit width of 5 nm and the excitation wavelength of 400 nm. Time-resolved PL spectroscopy was performed on an FLS 920 spectrometer (Edinburg, UK) with the excitation wavelength of 404 nm and the monitoring wavelength of 460 nm. The decay curves were fitted to a triple-exponential model, $I(t) = B_1 \cdot \exp(-t/\tau_1) + B_2 \cdot \exp(-t/\tau_2) + B_3 \cdot \exp(-t/\tau_3)$, where I, t, τ_1–τ_3, and B_1–B_3 are the intensity, the time, the PL lifetimes, and the amplitudes of components, respectively [24]. The average PL lifetime (τ_m) was calculated via the equation, $\tau_m = (R_1 \cdot \tau_1^2 + R_2 \cdot \tau_2^2 + R_3 \cdot \tau_3^2)/(R_1 \cdot \tau_1 + R_2 \cdot \tau_2 + R_3 \cdot \tau_3)$, where R_1–R_3 are the percentages of τ_1–τ_3, respectively [25].

2.3. Photoelectrochemical tests

Photoelectrochemical experiments were conducted on a Chenhua CHI660E electrochemical workstation (China) connecting with a three-electrode system comprising a working electrode, a counter electrode (Pt sheet), and a reference electrode (Ag/AgCl). For preparation of the working electrode, the sample (20 mg) and ethylene glycol (400 μL) were ground together for 2 min in a mortar and taken to coat the marked region (1 cm × 1 cm) on a piece of clean ITO glass by the doctor-blade method. The electrode was dried at 60 °C for 12 h and calcined at 200 °C for 2 h in the N_2 atmosphere. The potential (vs. Ag/AgCl) was adjusted to that (vs. SHE) via the equation, E_{SHE} (V) = $E_{Ag/AgCl}$ (V) + 0.197 V. Photocurrent density was tested at a bias voltage of − 0.3 V in the 0.2 M Na_2SO_4 solution. A 300-W Xe lamp (CEL-HXF300, Ceaulight, China) equipped with a cutoff filter ($\lambda \geq$ 420 nm) was used as the visible light source. Electrochemical impedance spectroscopy (EIS) was performed in the 0.1 M KCl solution including 2.5 mM $K_3Fe(CN)_6$ and 2.5 mM $K_4Fe(CN)_6$, with a frequency range of 0.01–10^4 Hz, an AC voltage of 5 mV, and a bias voltage of 0.2 V.

2.4. Theoretical calculations

The first-principles were employed to perform all density functional theory (DFT) calculations within the generalized gradient approximation (GGA) using the Perdew-Burke-Ernzerhof (PBE) [26] formulation. The projected augmented wave (PAW) potentials [27–29] were chosen to describe the ionic cores and valence electrons were taken into account using a plane wave basis set with a kinetic energy cutoff of 500 eV. The electronic energy was considered self-consistent when the energy change was < 10^{-5} eV. A geometry optimization was considered convergent when the energy change was < 0.02 eV $Å^{-1}$. The Brillouin zone integration was performed using 2 × 2 × 2 Monkhorst-Pack k-point sampling for a structure.

Formation energy (E_F) of the surface Ov on samples was calculated

by $E_F = E_{tot}$(with Ov) + E(O) − E_{tot}(without Ov), where E_{tot}(with Ov), E(O), and E_{tot}(without Ov) are the total energy of the model with an Ov, the energy of one O atom, and the total energy of the model without the Ov, respectively.

2.5. Photocatalytic nitrogen fixation

The photocatalyst (50 mg) was dispersed in pure water (80 mL) by sonification for 5 min and then transferred into the reactor connecting with a circulating water-cooling system to control the temperature of 20 °C. The dispersion was magnetically stirred in the dark with high-purity N_2 bubbling (300 mL min^{-1}) for 30 min to saturate the solution with N_2 dissolution and drive away the oxygen in the reactor. Then, A 300-W xenon lamp (CEL-HXF300-T3, Ceaulight) equipped with a cutoff filter ($\lambda \geq 420$ nm) was used as the visible light source to start the reaction. Some dispersion (5 mL) was taken out every 20 min and centrifuged at 10000 rpm to separate the photocatalyst. Finally, the supernatant (4 mL) was taken to measure the ammonia concentration by the Nessler's reagent spectrophotometry method [30] using the Shimadzu UV-1800 UV-vis spectrophotometer (Japan). The standard curve for the absorbance vs. the concentration of ammonium associated with Nessler's reagent is shown in Fig. S1. To investigate the possible influence of H_2O_2, BMO80 was dispersed and stirred in the H_2O_2 solution (~0.14 g L^{-1}, 80 mL) for 1 h in the dark, and then collected by filtration, washed with water and used for photocatalytic N_2 reduction. To investigate the effect of hydroxyl radicals, the t-butyl alcohol aqueous solution (137.5 mg L^{-1}, 80 mL) was substituted for the pure water (80 mL). To eliminate the influence of holes, the pure water (80 mL) was replaced with the methanol aqueous solution (10 vol%, 80 mL), and the N_2 atmosphere was further replaced with air to investigate the influence of O_2.

To confirm the apparent quantum yield (AQY), the NH_3 production rate (R_N) was measured under monochromatic light derived by substituting a 400-, 420-, 450-, or 480-nm band-pass filter (Thorlabs, USA) for above cutoff filter. The AQY was calculated by the equation, AQY = $3R_N/(E_i \cdot A/E_p) \times 100\%$, where E_i is the incident light intensity minus the transmission light intensity (W cm^{-2}), A is the illumination area (cm^2), and E_p is the photon energy (J mol^{-1}).

2.6. ^{14}N and ^{15}N isotope labeling experiments

The isotope labeling experiments of BMO80 were conducted on a

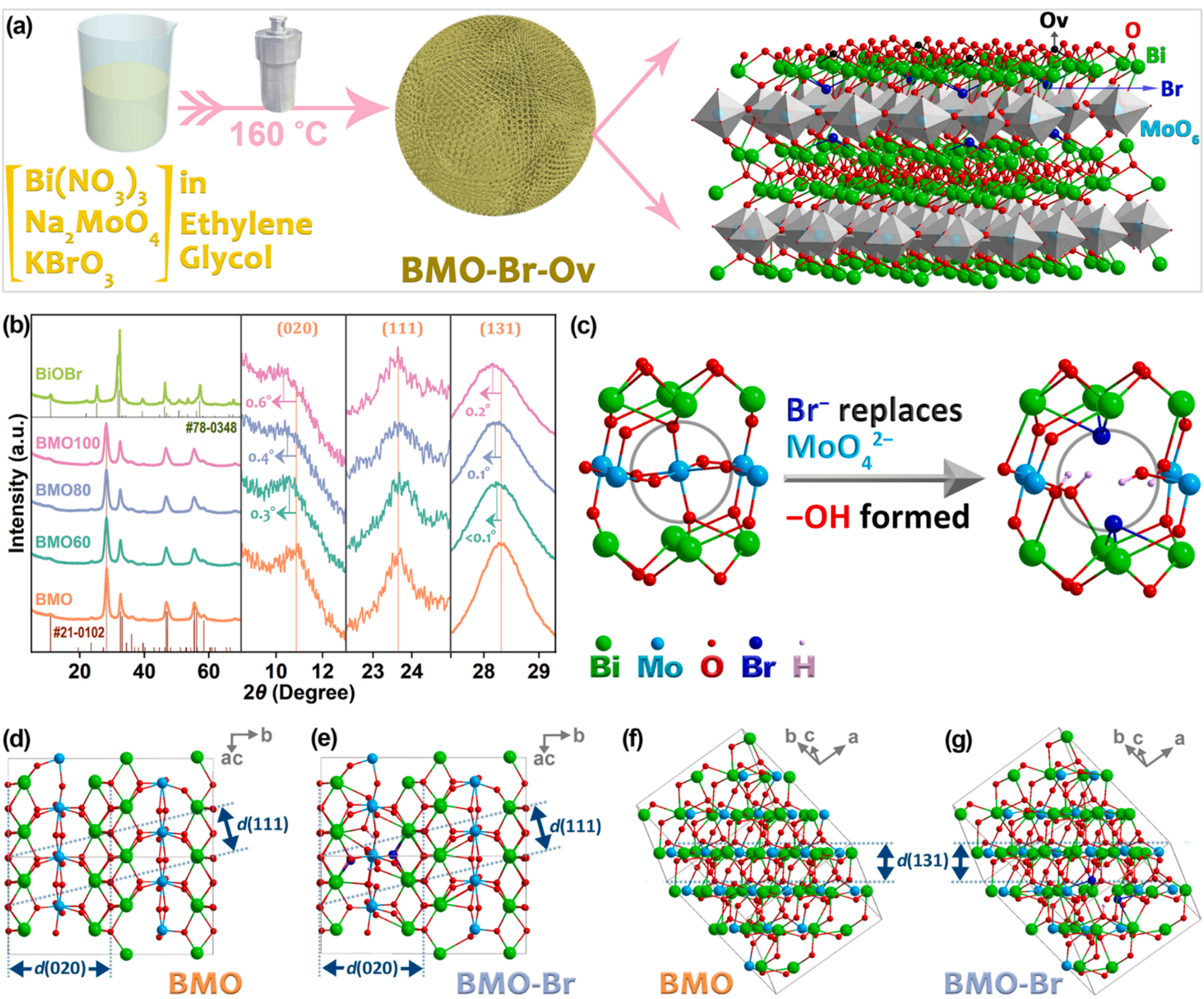

Fig. 1. (a) Schematic illustration for the synthesis and structure of BMO-Br-Ov; (b) XRD patterns of the samples; (c) the microstructure of Br doped BMO (BMO-Br) with Br^- replacing original MoO_4^{2-} groups and OH formed; and (d and e) marked (020) and (111) facets and (f and g) marked (131) facets in optimized crystal structures of (d and f) BMO and (e and g) BMO-Br.

CEL-SPH2N-D photoactivity-evaluation system (Ceaulight, China). The photocatalyst (50 mg) was dispersed into ultrapure water (40 mL) in the reactor which was then connected to the evaluation system. The system was evacuated, followed with Ar (~40 mL) injected, and this procedure was repeated three times to completely remove the air. Afterwards, $^{14}N_2$ or $^{15}N_2$ (~40 mL) was injected into the reactor. The nitrogen reduction was started under irradiation of a 300-W xenon lamp ($\lambda \geq 420$ nm) and lasted for 10 h. For ^{1}H nucleus magnetic resonance (NMR) measurement, the reaction solution was filtered, acidized to pH of 2 by hydrochloric acid, and concentrated to ~3 mL by rotary evaporation at 50 °C. Then, the concentrated solution (0.2 mL) was mixed with d_6-DMSO (0.6 mL) for the ^{1}H NMR spectroscopy measurement.

3. Results and discussion

3.1. Structure, morphology, and composition

Fig. 1a shows the synthesis of BMO-Br-Ov via a simple solvothermal process with BrO_3^- as the source of the Br dopant. Crystallinity of samples was first evaluated by XRD. As shown in Fig. 1b, BMO and BiOBr exhibit typical diffraction peaks of reported bismuth molybdate with an orthorhombic structure (JCPDS No. 21–0102) [31] and bismuth oxybromide with a tetragonal structure(JCPDS No. 78–0348) [32], respectively, indicative of reduction of BrO_3^- to Br^-. BMO*x* exhibits similar diffraction peaks as BMO, suggesting no detectable new crystal phases were formed. However, the enlarged patterns of BMO*x* show gradually increased shift of (020) and (131) peaks to low 2θ (indicative of increased crystal facet spacings) and unchanged (111) peak position with increasing *x*, relative to those of BMO, effectively verifying the Br doping in BMO*x*. From BMO to BMO80, the (131) peak shifts from 28.3° to 28.2° with the facet spacing increasing from 3.15 to 3.16 Å. To exclude the possible influence of surface Ov on the crystallinity, X-ray diffraction (XRD) patterns of the samples after calcined at 300 °C in air for 2 h (eliminating surface Ov [33]) were also measured. Both BMO and BiOBr exhibit similar diffraction peaks before and after the calcination (Fig. S2), and (020) and (131) peaks of BMO*x* still show increased shift to the low 2θ with increasing *x* and the (111) peak position stays constant (Fig. S3), further demonstrating the influence of Br doping in BMO*x*. Besides, BMO (containing Ov generated by reduction of ethylene glycol [34]) exhibits prominent shift of (020) and (131) peaks to the low 2θ, compared with BMO-H_2O (hardly containing Ov [34]) (Fig. S2a), suggesting the bulk Ov can also cause the increase of crystal facet spacings.

The proposed Br doping mechanism is shown in Fig. 1c. According to the stoichiometric ratio, it is probable that two Br^- replace one MoO_4^{2-}, with OH coordination balancing the crystal structure. Based on the proposed mechanism of Br doping in BMO, the optimized Br-doped BMO (BMO-Br) structure and the BMO structure are shown in Fig. 1d–g. Apparently, the Br^- substitution for MoO_4^{2-} can effectively cause increase of (020) and (131) facet spacings and hardly cause variation of the (111) facet spacing of BMO-Br, in light of its layered structure and Bi−O−Mo and Bi−Br bonding direction, which demonstrates rationality of the proposed Br doping structure.

Morphologies of samples were observed by SEM and TEM. BMO and BMO80 comprise similar hierarchical microspheres composed of small nanosheets while BiOBr consists of hierarchical microspheres composed of relatively large nanosheets (Fig. 2a–c and S4), indicating the Br doping did not cause variation of the basic morphology and there was no BiOBr formed in BMO80. EDS elemental analysis (Fig. S5) and elemental mapping images (Fig. 2d) of BMO80 show homogeneous distribution of

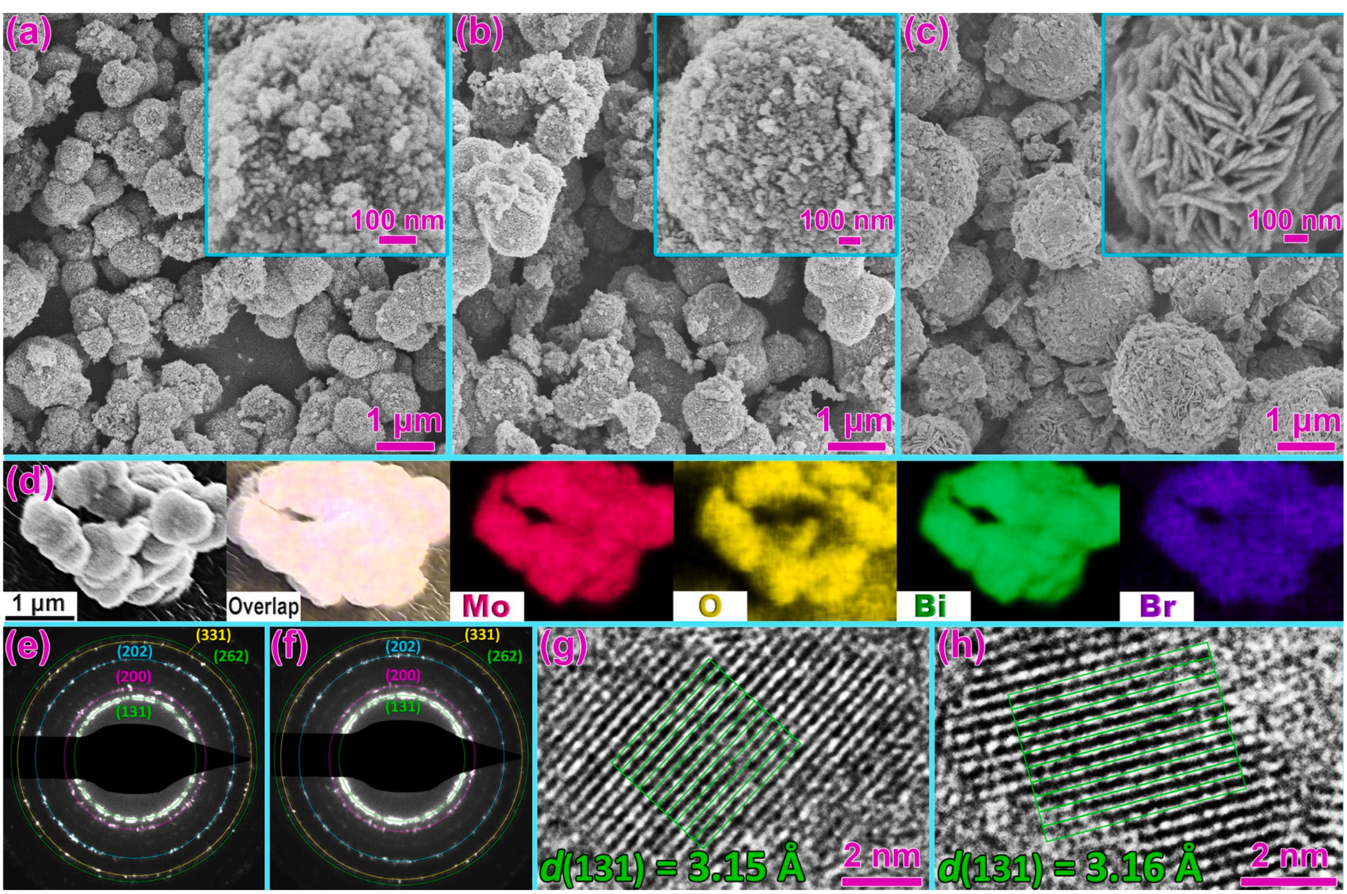

Fig. 2. SEM images of (a) BMO, (b) BMO80, and (c) BiOBr; (d) EDS elemental mapping images of BMO80; SAED patterns of (e) BMO and (f) BMO80; and HRTEM images of (g) BMO and (h) BMO80.

Bi, Mo, O, and Br elements in the sample, further suggesting the doping of Br rather than formation of large BiOBr nanosheets in BMO80. SAED and HRTEM were further performed to evaluate crystal structures of BMO and BMO80. As shown in Fig. 2e and f, SAED patterns.

of BMO and BMO80 reveal similar diffraction rings composed of diffraction spots, indicating similar exposed facets of small single-crystal nanosheets in BMO and BMO80, consistent with the SEM and TEM results. Furthermore, crystal lattice fringes could be clearly observed in HRTEM images of BMO and BMO80 (Fig. S6), manifesting the high crystallinity of the small nanosheets. Fig. 2g and f shows lattice fringes with spacings of 3.15 and 3.16 Å, respectively, corresponding to (131) facets of BMO and BMO80. This small spacing difference may arise from the Br doping, rather than the measurement error, based on our repetitive measurement (Fig. S7), which accords well with the XRD results.

Electron paramagnetic resonance (EPR) spectroscopy was performed to determine defects in the samples. As shown in Fig. 3a, BMO, BMO80, and BiOBr exhibit symmetric EPR signals at *g* of about 2.003, attributed to electrons trapped on the Ov [35–37]. The EPR signal of BMO80 is much stronger than those of BMO and BiOBr in the dark, indicating its higher Ov content, i.e., the Br doping enhances the Ov generation in BMO80. Under light irradiation, the signal enhancement of the samples results from photoexcited electrons [38] and the enhancement also follows the order, BMO < BiOBr < BMO80, manifesting the enhanced Ov content benefits charge photoexcitation [39]. To further investigate the Ov distribution in the samples, EPR spectra of BMO and BMO80 after calcined at 300 °C in air for 2 h (marked as BMOc and BMO80c) were also measured (Fig. 3b). Compared with the EPR signals of BMO and BMO80 in the dark (Fig. 3a), the signal of BMOc decreases slightly while that of BMO80c decreases substantially to turn basically as strong as the signal of BMOc, suggesting the Ov distributes both in the bulk and on the surface of BMO and the Br-doping generated Ov in BMO80 exists mainly on the surface. The signal enhancement of BMOc and BMO80c under light irradiation is lower than that of BMO and BMO80, further indicating the reduction of surface Ov.

X-ray photoelectron spectroscopy (XPS) was conducted to further confirm the structures of samples. Fig. 3c shows Bi 4 f core-level XPS spectra of BMO, BMO80, and BiOBr. Three couples of peaks were obtained for BMO after deconvolution. The peaks at binding energy (BE) of 164.4 and 159.1 eV are ascribed to 4 $f_{5/2}$ and 4 $f_{7/2}$ of Bi^{3+} in Bi−O of Bi_2MoO_6 [40], while the couple of peaks at 163.8 and 158.6 eV ascribed to Bi with Ov (simply marked as Bi^{2+}) [18]. The last couple of peaks at higher BE (165.0 and 159.7 eV) should correspond to Bi^{3+} in surface

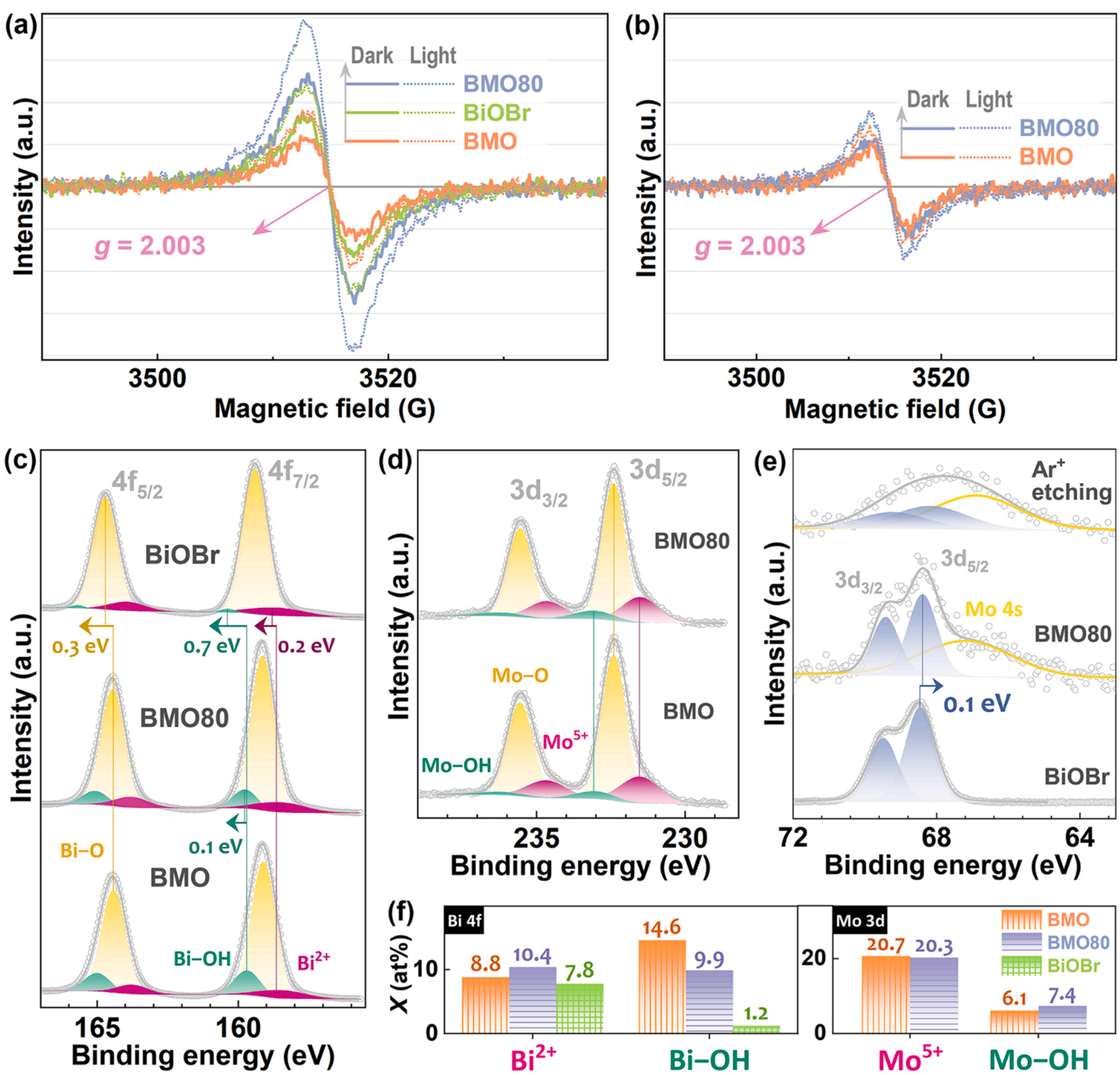

Fig. 3. (a) EPR spectra of BMO, BMO80, and BiOBr in the dark and under visible light irradiation; (b) EPR spectra of the samples after calcined at 300 °C in air for 2 h; (c) Bi 4 f core-level XPS spectra of the samples; (d) Mo 3d core-level XPS spectra of BMO and BMO80; (e) Br 3d core-level XPS spectra of BiOBr, BMO80, and BMO80 after Ar^+ etching; and (f) molar content (*X*) of Bi species in Bi element and Mo species in Mo element, calculated according to the XPS data.

Bi−OH [41]. BMO80 exhibits similar three couples of peaks as BMO, suggesting similar crystal structure, except the 0.1-eV shift of "Bi−OH" peaks to high binding energy, caused by the Br doping. The three couples of peaks for BiOBr all lie at remarkably higher BE than those for BMO, owing to difference of chemical environment. Fig. 3d shows Mo 3d core-level spectra of BMO and BMO80. BMO80 exhibits similar three couples of peaks as BMO, i.e., two peaks at 235.6 and 232.4 eV corresponding to $3d_{3/2}$ and $3d_{5/2}$ of Mo^{6+} in M−O of Bi_2MoO_6 [40], the couple of peaks at 234.7 and 231.5 eV ascribed to Mo with Ov (simply marked as Mo^{5+}) [42], and the last couple at higher BE (236.3 and 233.1 eV) assigned to Mo^{6+} in surface Mo−OH. Fig. 3e shows Br 3d core-level spectra of BiOBr and BMO80. Two peaks at 69.5 and 68.5 eV for BiOBr are assigned to $3d_{3/2}$ and $3d_{5/2}$ of Br^- in BiOBr [43]. BMO80 exhibits similarly two peaks as BiOBr but with ~0.1-eV shift to the low BE owing to the difference of chemical environment of Br, and these two peaks for BMO80 after Ar^+ etching turn considerably weak, indicating Br^- mainly lies in the surface. In addition, BMO and BMO80 exhibit similar peaks in the O 1 s core-level spectra, further indicative of their similar crystal structure, and the peaks of BiOBr shift to the high BE (Fig. S8) because of the difference of chemical environment.

Based on the XPS peak area (Table S1), molar content (X) of Bi and Mo species in Bi and Mo elements were calculated, respectively. As shown in Fig. 3f, BMO80 possesses greater $X(Bi^{2+})$ (10.4%) than BMO and BiOBr (8.8% and 7.8%), indicating the Br doping enhanced Ov generation at Bi. Moreover, BMO80 possesses remarkably smaller X (Bi−OH) (9.9%) than BMO (14.6%), suggesting generation of new Ov was accompanied with reduction of surface OH, i.e., the Br doping induced generation of surface Ov, consistent with the EPR results. Meantime, the $X(Mo^{5+})$ of BMO80 (20.3%) approximately equals to that of BMO (20.7%), indicating the Br doping did not induce generation of new surface Ov at Mo, which is also reflected by similar Mo 3d peak positions of BMO and BMO80 (Fig. 3d). For BMO and BMO80, the calculated Bi^{2+}/Mo^{5+} molar ratios are ~0.82 and 1.12, respectively. The 0.82 < 1 indicates the bulk Ov lies a little more at Mo than at Bi, and the 1.12 > 0.82 indicates the new generated surface Ov mainly lies at Bi. BMO80 exhibits greater X(Mo−OH) (7.4%) than BMO (6.1%), effectively evidencing the additional OH coordination when Br^- replacing MoO_4^{2-} or the rationality of proposed Br doping mechanism in BMO80 (Fig. 1c).

The distribution of new generated Ov only on surfaces of BMO80 probably results from Br doping in the surface layer. The Mo/Bi molar ratios of BMO and BMO80 were determined to be 0.499 and 0.489, respectively, by ICP-OES, close to their theoretical values (0.50 and 0.48). The Br content cannot be exactly measured by ICP-OES owing to inevitable loss in the measuring process. The calculated Mo/Bi molar ratios of BMO and BMO80, based on the XPS data (Table S1), are 0.494 and 0.434, respectively. Apparently, these two methods give similar values for BMO, indicating reliability of the methods. Then, for BMO80, the prominently smaller value (0.434) from the XPS data (with detecting depth of <10 nm) than that determined by ICP-OES (0.489) demonstrates the surface-layer Br doping by replacing MoO_4^{2-}. In addition, the calculated Br/(Mo + Bi) molar ratio from the XPS data for BMO80, ~0.0308 is remarkably higher than the theoretical value (0.0270), also indicating the surface-layer Br doping. The reason for Br doping in the surface layer rather than in the bulk maybe arise from the higher stability of Mo−O−Bi than that of Br−Bi which leads to first nucleation and growth of Bi_2MoO_6, as evidenced by the fact that BiOBr dispersed in the MoO_4^{2-} solution could turn into Bi_2MoO_6 in the hydrothermal process (Fig. S9).

3.2. Properties and energy band structures

Thermal decomposition properties of samples were investigated (Fig. 4a). Thermogravimetric (TG) analysis and corresponding differential scanning calorimetry (DSC) analysis on BMO roughly show two endothermic decomposition steps, i.e., at temperature (T) of < ~170 °C and at 170 °C < T < 480 °C, ascribed to evaporation of surface adsorbed free water [44] and removal of chemically adsorbed species (e.g., N_2, O_2, and H_2O) at the Ov sites [45], respectively. For BMO80, the weight loss at the second step is remarkably larger than that for BMO, suggesting there are more Ov in BMO80, consistent with the EPR and XPS results. In addition, there is the third decomposition step for BMO80 at 580 °C < T < 710 °C with a weight loss of ~0.6%, which should be ascribed to the removal of partial Br^-. The Br^- removal temperature for BMO80 is much higher than that for BiOBr (510 °C < T < 670 °C, Fig. S10), because the Br doping structure in BMO80 is different from the BiOBr structure. Fig. 4b shows N_2 temperature-programmed desorption (N_2-TPD) curves of BMO, BMO80, and BiOBr. Peaks at 200 °C < T < 450 °C for BMO should be ascribed to N_2 adsorption [18], and three peaks at ~255, 309, and 374 °C likely correspond to chemical adsorption of N_2 at different surface Ov sites. For BMO80, similar three peaks (at ~273, 337, and 424 °C) can be observed, but with higher intensity and T (as shown by solid lines), indicating BMO80 possesses the higher capability to chemisorb and activate N_2 than BMO [18]. BiOBr exhibits two peaks at 263 and 409 °C, lower than those of BMO80, and especially, the intensity of the peak at 409 °C is much lower than the peak of BMO80 at ~424 °C, indicating its relatively low ability in N_2 chemisorption.

N_2 sorption isotherms of the samples were measured to characterize their mesoporous structures. As shown in Fig. 4c, the N_2 adsorption amount of the samples follows the sequence, BMO80 > BMO > BiOBr, revealing the highest N_2 adsorption ability of BMO80, consistent with

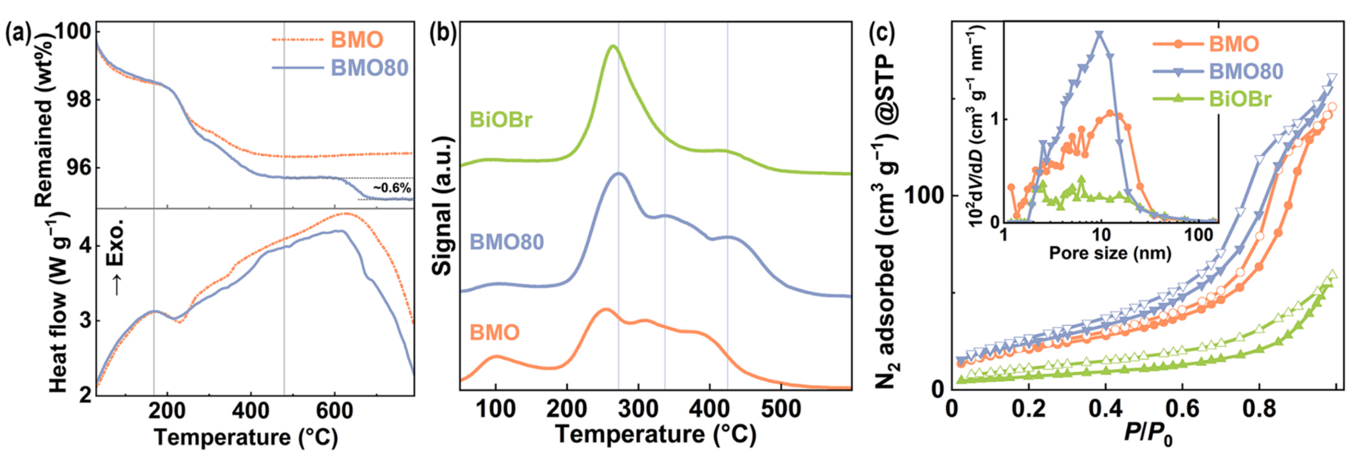

Fig. 4. (a) TG and DSC curves of BMO and BMO80; (b) N_2-TPD curves of BMO, BMO80, and BiOBr; and (c) N_2 sorption isotherms and (Inset) pore-size distribution curves of the samples.

the TPD results, which favors the surface catalytic reaction of N_2. All the samples exhibit type-IV isotherms featured with type-H3 hysteresis loops, demonstrating their mesoporosity [46]. The BET specific surface area of BMO, BMO80 and BiOBr are 75.9, 89.5, and 25.6 $m^2\ g^{-1}$, respectively. Pore-size distribution curves of the samples show mesopores with size of ~2–30 nm and their pore volume follows the order, BMO80 (0.25 $cm^3\ g^{-1}$) > BMO (0.23 $cm^3\ g^{-1}$) > BiOBr (0.09 $cm^3\ g^{-1}$). Apparently, BMO80 possesses the largest surface area and pore volume, benefiting surface reaction and mass transfer.

Optical absorption performance of the samples was evaluated by UV–vis diffuse reflectance spectroscopy (DRS). BMO, BMO80, and BiOBr all exhibit the Urbach tail absorption (Fig. S11) because of surface Ov [47]. More surface Ov for BMO80 leads to its slightly higher visible light absorption. The absorption edges (λ_{ed}) of BMO, BMO80, and BiOBr were determined to be ~498, 507, and 436 nm, respectively (Fig. S11) and their bandgaps ($E_g = 1240/(\lambda_{ed}/\text{nm})$ eV [48]) were roughly calculated to be 2.49, 2.45, and 2.84 eV. Valence band (VB) edges (E_{VB}) of BMO, BMO80, and BiOBr were determined as 2.05, 2.06, and 2.93 eV (vs. SHE), respectively, by ultraviolet photoelectron spectroscopy (UPS) (Fig. S12). Then, their conduction band (CB) edges ($E_{CB} = E_{VB} - E_g$) are calculated to be − 0.44, − 0.39, and 0.09 eV, respectively. Preliminary energy band structures of the samples are shown in Fig. 5a. Apparently, the Br doping in BMO80 causes negligible shift of E_{VB}, but downshift of E_{CB} in comparison with those of BMO. Fermi levels (E_f) of the samples were further confirmed by VB-XPS. As shown in Fig. 5b, the ($E_{VB} - E_f$) [49] for BMO, BMO80, and BiOBr is determined as 2.07, 2.13, and 2.18 eV, respectively, i.e., their E_f is − 0.02, − 0.07, and 0.75 eV. BMO80 exhibits the E_f closer to E_{CB} than BMO (Fig. 5a), suggesting a higher n-type dopant concentration [50] in BMO80, and the n-type dopants here are likely Ov and Br.

DFT calculations were performed to investigate influences of Ov modification and Br doping on energy band structures of Bi_2MoO_6. Fig. 6a–d shows optimized configurations of Bi_2MoO_6, Ov modified Bi_2MoO_6 (BMO-Ov), Br doped Bi_2MoO_6 (BMO-Br), and Ov modified and Br doped Bi_2MoO_6 (BMO-Br-Ov), respectively. The Ov position was set, as shown by arrows in the figure, based on the principle that the Ov in BMO-Br-Ov is located at Bi close to Br. The stable existence of BMO-Br-Ov reveals the rationality of the structure of BMO80 we proposed (Fig. 1). Fig. 6e shows the calculated energy band and density of state (DOS) plots of Bi_2MoO_6. The E_g was determined as 2.11 eV, with the CB edge composed of the Mo 4d orbital (main) and the O 2p orbital and the VB edge composed of the O 2p orbital (main) and the Bi 6 s orbital (Fig. S13). BMO-Ov (Fig. 6f) exhibits the E_g of 2.14 eV, similar to that of Bi_2MoO_6, suggesting the Ov modification causes no remarkable variation of E_g, but there is apparently an impurity level, close to the CB edge, consisting of the Bi 6 s orbital (main), the O2p orbital (main), and the Mo 4d orbital, which reduces the apparent E_g to 1.56 eV. The doping level should arise from the Ov at Bi (Fig. 6b). Relative to the CB edge of Bi_2MoO_6, that of BMO-Ov approaches more to the Fermi level, indicating the n-type doping of Ov, consistent with the experimental result (Fig. 5a). BMO-Br (Fig. 6g) exhibits the E_g of 1.80 eV, narrower than that of Bi_2MoO_6, indicating the Br doping can remarkably decrease the bandgap. Though the Br doping mainly contributes to the DOS of the VB edge, it also causes the CB edge prominently to approach to the Fermi level probably by affecting adjacent Bi, compared with the band levels of Bi_2MoO_6 (Fig. 6e), manifesting the n-type doping nature of Br. The E_g of BMO-Br-Ov (1.86 eV) is close to that of BMO-Br, further indicating the Ov causes negligible variation of the bandgap, but there is also an impurity level, approaching to the CB edge, mainly contributed by the Bi 6 s orbital and the O 2p orbital, indicating the significant role of Ov at Bi. Besides, the CB edge of BMO-Br-Ov approaches more to the Fermi level than that of BMO-Ov, further indicative of the influence of adjacent Br.

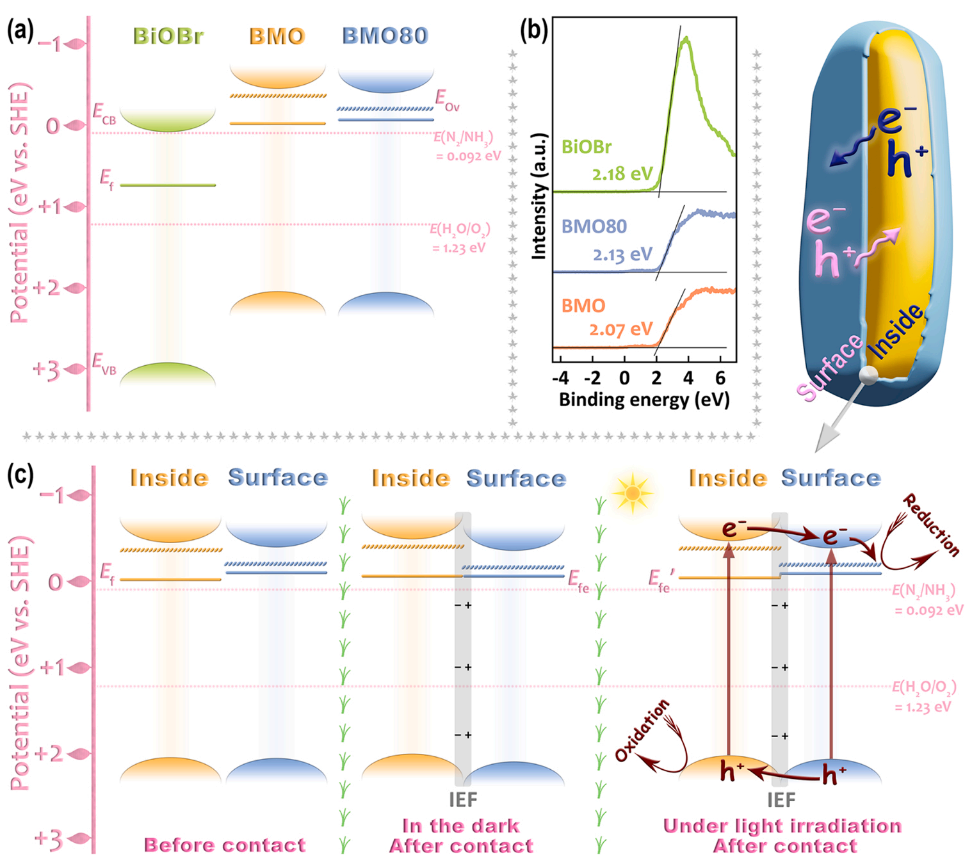

Fig. 5. (a) Energy band levels of BMO, BMO80, and BiOBr; (b) VB-XPS spectra of the samples; and (c) schematic illustration for fabrication of inside/surface homojunction in BMO80 based on the band levels. "IEF" represents interfacial electric field.

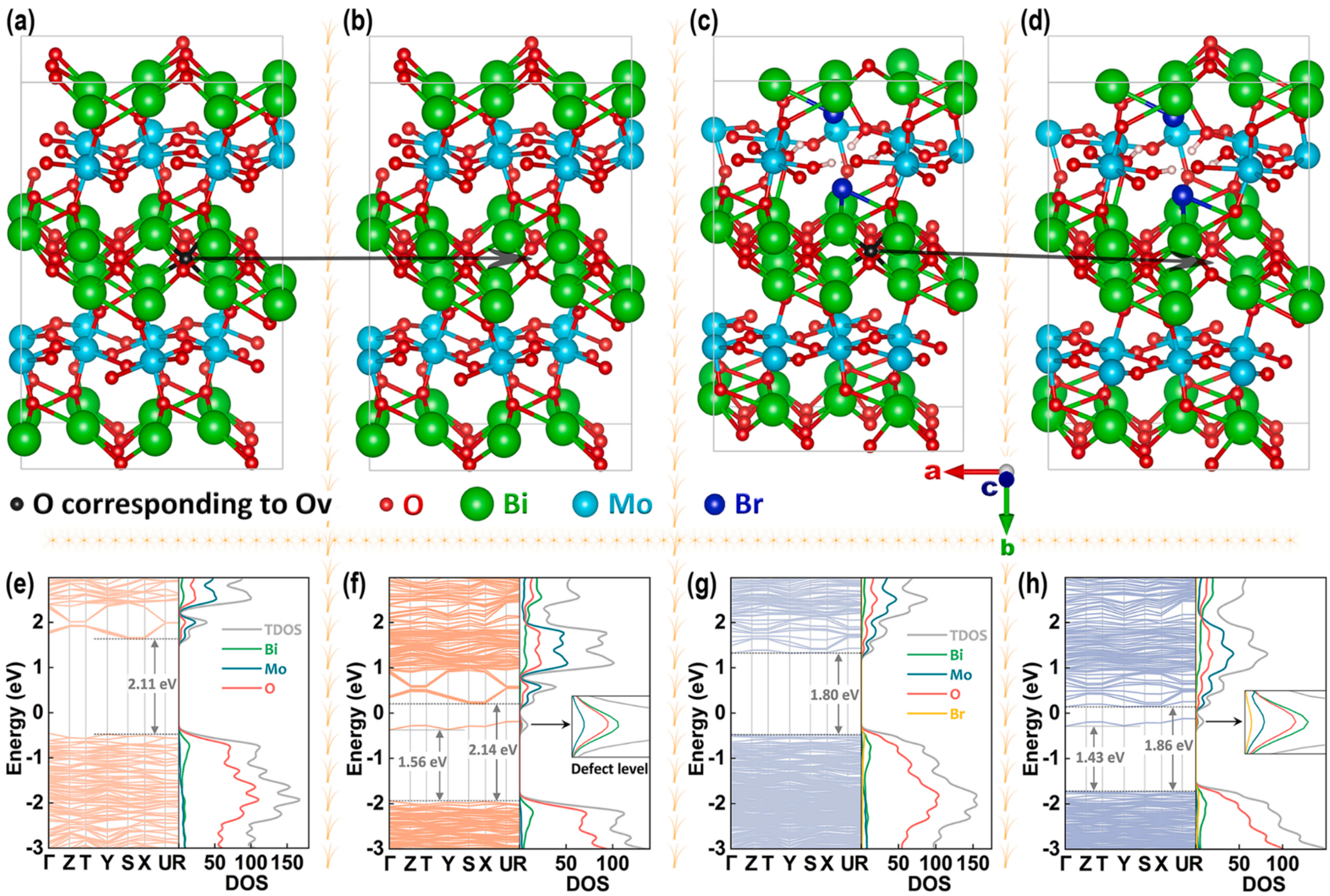

Fig. 6. Optimized structural models of (a) Bi_2MoO_6, (b) Ov modified Bi_2MoO_6 (BMO-Ov), (c) Br doped Bi_2MoO_6 (BMO-Br), and (d) Ov modified and Br doped Bi_2MoO_6 (BMO-Br-Ov); and corresponding plots of energy bands and density of states (DOS) for (d) Bi_2MoO_6, (e) BMO-Ov, (f) BMO-Br, and (g) BMO-Br-Ov. The Fermi levels were set at 0.

According to above calculation results, it can be concluded that the Ov modification can induce a defect level (E_{Ov}) close to the CB edge in the bandgap (Fig. 5a), favoring the optical absorption and photogenerated charge separation [51], that the downshift of E_{CB} of BMO80 relative to that of BMO (Fig. 5a) arises from the Br doping, and that both Ov and Br work as the n-type dopants to facilitate photoexcitation of electrons to participate in the interfacial reduction reaction. It should be noted that the shallow E_{Ov} can capture photoexcited electrons at the CB and work as active centers to enhance the interfacial reduction reaction, however, excessive Ov will turn E_{Ov} into a deep level that traps the electrons and slows the interfacial reaction. Therefore, there is an optimal Ov concentration (i.e., the Br doping concentration) for BMO-Br-Ov. To clarify the reason for more surface Ov generation in BMO80 than in BMO, formation energy (E_F) of surface Ov in BMO-Ov and BMO-Br-Ov (Fig. S14) was calculated. The E_F for BMO-Br-Ov (1.73 eV) is lower than that for BMO-Ov (1.87 eV), indicating that the Br doping promotes formation of surface Ov at adjacent Bi, consistent with the XPS results.

The different band levels of BMO80 from those of BMO suggest band levels of the surface layer of BMO80 are different from those of the inside which can be considered similar to those of BMO. Therefore, E_f of the surface layer of BMO80, determined by the VB-XPS, should approach more to E_{CB} than the average E_f of BMO80, as shown in Fig. 5c. The contact of the surface layer and the inside would be accompanied with electron transfer from the surface-layer to the inside till the equilibrium E_f (E_{fe}) was formed, and lead to fabrication of an interfacial electric field (IEF). Under light irradiation, the IEF can effectively promote photogenerated electron transfer from the inside to the surface layer and hole transfer on the opposite direction with a quasi-equilibrium E_f (E_{fe}') formed, suggesting fabrication of the inside/surface homojunction in BMO80 (Fig. 5c). The electrons may further transfer to E_{Ov} to reduce chemisorbed N_2. On the whole, the homojunction and Ov may considerably enhance the photogenerated charge separation.

To evaluate the charge separation performance of the samples, photoluminescence (PL) spectra of BMO, BMO80, and BiOBr were measured (Fig. 7a). BMO80 exhibits much lower PL intensity than BMO and BiOBr, suggesting the smallest photogenerated charge recombination efficiency [38] which should result from the surface/inside homojunction and fast transfer of electrons to the defect level. PL lifetimes of the samples were determined by time-resolved fluorescence spectroscopy. As shown in Fig. 7b, all the decay curves can be well fitted.

to a tri-exponential model. The three lifetimes ($\tau_1 - \tau_3$) and their mean lifetime (τ_m) of BMO80 are all lower than those of BMO and BiOBr, suggesting the decreased radiative recombination of photogenerated charge carriers, which likely results from the rapid charge transfer across the surface/inside homojunction and the following transfer of electrons from the CB to the defect level, decreasing the direct charge recombination, with subsequent nonradiative energy conversion [52]. Fig. 7c shows photocurrent response of the samples. Apparently, BMO80 exhibits larger increase in cathodic current density (~6.3 μA cm^{-2}) than BMO and BiOBr (~2.5 and 2.4 μA cm^{-2}) under visible light irradiation, indicating its higher photogenerated charge separation efficiency [53]. Electrochemical impedance spectroscopy (EIS) was performed to evaluate the charge transfer capability of the samples. As shown in Fig. 7c, the EIS spectra of BMO, BMO80, and BiOBr can be well fitted by the provided equivalent circuit, and the obtained charge transfer resistance

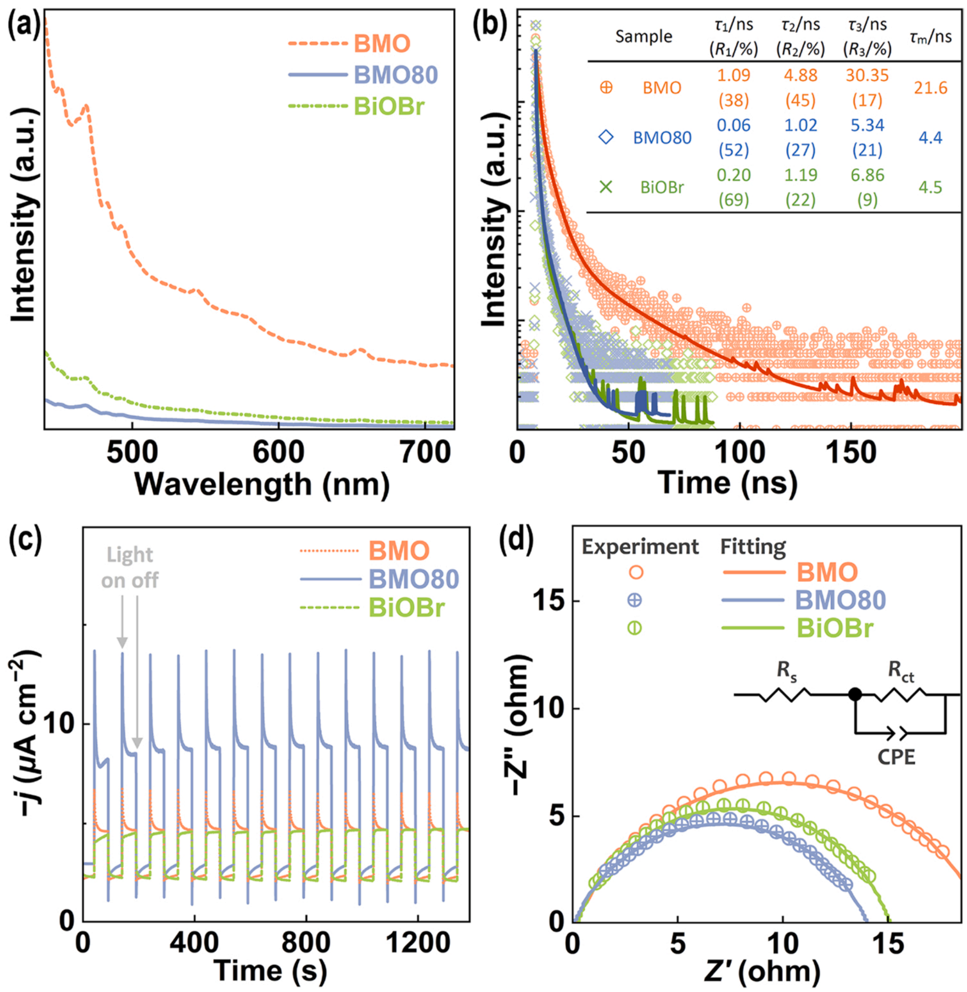

Fig. 7. (a) Photoluminescence spectra of BMO, BMO80, and BiOBr; (b) time-resolved fluorescence spectra of the samples; (c) cathodic current density of the samples in the dark and under visible light ($\lambda \geq 420$ nm) irradiation; and (d) electrochemical impedance spectra of the samples under visible light irradiation. The data in (b) are obtained by fitting the decay curves to a tri-exponential model. The data in (d) were well fitted by the provided equivalent circuit where R_s, R_{ct}, and CPE represent the solution resistance, the charge transfer resistance, and the double-layer capacitance, respectively.

(R_{ct}) of the samples are 19, 14, and 15 Ω, respectively. The lowest R_{ct} of BMO80 suggests its highest charge transfer ability [54]. Overall, the high photogenerated charge separation and transfer performance of BMO80 is favorable for enhancement of its photocatalytic nitrogen reduction activity.

3.3. Photocatalytic nitrogen fixation and related mechanism

Photocatalytic nitrogen reduction performance of BMO_x, BMO, and BiOBr in pure water (Fig. 8a and b) was first evaluated. The NH_3 was gradually produced with time for all the samples (Fig. 8c), indicative of the photocatalytic process. Fig. 8d shows the NH_3 production rates (R_N) of the samples. BMO80 exhibits the highest R_N (1.60 μmol h^{-1}) among BMO*x*, indicating the optimal Br doping amount in BMO80, which is ~2.5 and 2.0 times higher than that of BMO and BiOBr, respectively, suggesting the superiority of BMO80 with more Ov. The decisive role of Ov can be further verified by the fact that R_N of BMO80 and BMO are ~23 and 10 times that (0.07 μmol h^{-1}) of BMO-H_2O almost without Ov [34], respectively (Fig. 8d). BMO100 may possess more defective sites because of more Br doping, as shown by the XRD result (Fig. 1b), but excessive defects may work as charge recombination centers [52] and decrease its photoactivity. Fig. 8e shows apparent quantum yields (AQYs) of photocatalytic N_2 reduction on BMO80 at different wavelengths. The AQY at 420 nm reaches 0.52% and the reaction can proceed till the wavelength of 500 nm. Along with the UV–vis spectrum, the AQYs decrease gradually, indicative of the significant influence of optical absorption capability. Compared with reported photocatalysts, BMO80 exhibits relatively high AQYs (Table S2).

The specific surface area normalized R_N for BMO80, 0.36 μmol h^{-1} m^{-2}, is still ~2-fold higher than that (0.18 μmol h^{-1} m^{-2}) for BMO, indicating the surface area is not the key factor for the photoactivity enhancement. BMO80 exhibits only slightly higher visible light absorption than BMO, suggesting the optical absorption is not the key factor, either. Therefore, the enhanced photogenerated charge separation, benefiting from the surface Ov formation and the inside/surface homojunction fabrication, and the promoted N_2 chemisorption and activation at Ov should be responsible for the photoactivity enhancement, based on above discussion on properties and energy band structures.

The stability of BMO80 was investigated by the cyclic photocatalytic nitrogen reduction experiment. As shown in Fig. 8f, the photocatalytic activity of BMO80 decreases dramatically from the second run and remains only ~13% at the third run, revealing low stability of the sample. To disclose the reason for the low stability, methanol was added as the electron donor (eliminating holes) in the photocatalytic process (Fig. 8a), and BMO80 exhibits no decrease of photocatalytic activity in five-consecutive runs (Fig. 8g), manifesting its high stability. Meanwhile, the presence of methanol considerably accelerates the NH_3 production (Fig. 8g), with the R_N of 4.77 μmol h^{-1}, ~3 times that in pure water, and an AQY at 420 nm reaching 2.56% (Fig. 8e). These demonstrate that the low stability of BMO80 roots from the photogenerated holes.

The photochemical stability of BMO80 was further investigated by morphological and structural characterizations. SEM images of BMO80 after the cyclic experiments (Fig. S15) show similar hierarchical microspheres as that before (Fig. 2b), suggesting that the low

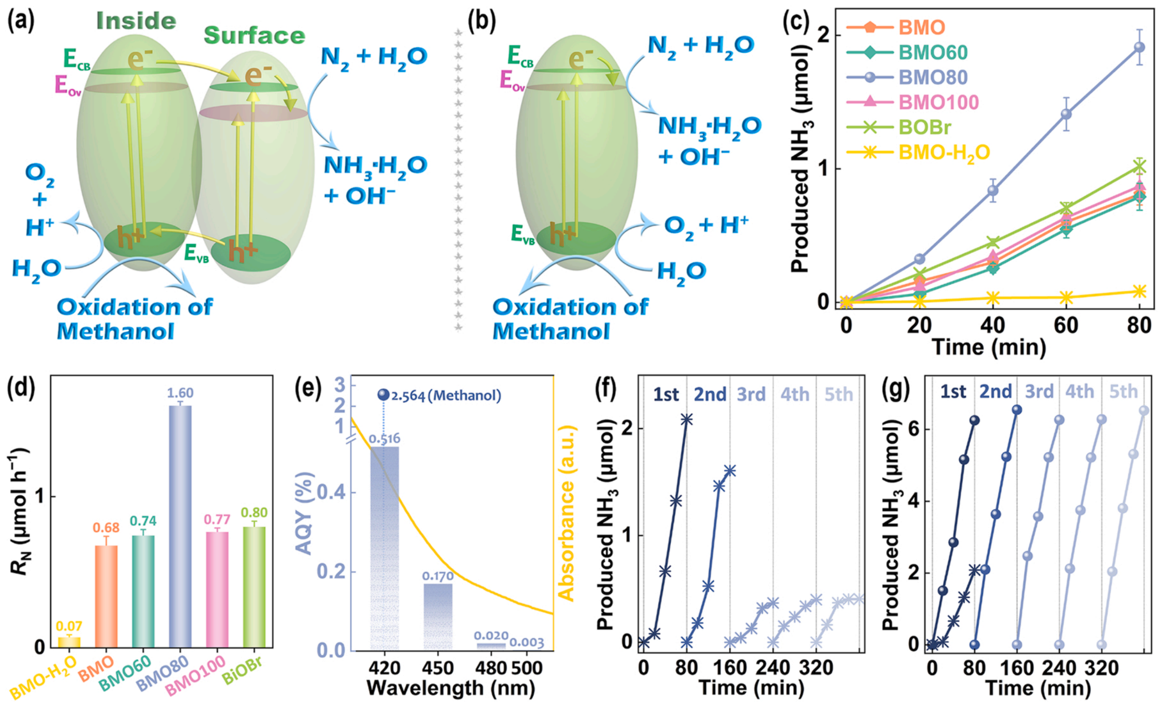

Fig. 8. Schematic illustration for photocatalytic N_2 reduction (a) on BMO_x and (b) on BMO and BiOBr in pure water or in the methanol solution; (c) time-dependent photocatalytic NH_3 production for various samples; (d) photocatalytic NH_3 production rates (R_N) of the samples; (e) apparent quantum yields (AQYs) of photocatalytic N_2 reduction on BMO80 at 420, 450, 480, and 500 nm in pure water and at 420 nm in the methanol solution; and the cyclic experiment of photocatalytic N_2 reduction on BMO80 (f) in pure water and (g) in the methanol solution.

photochemical stability of BMO80 in pure water does not arise from the morphological variation. BMO80 after the cyclic experiment in the methanol solution (marked as BMO80-After-M) exhibits a similar XRD pattern as that before (Fig. S16), indicative of high photochemical stability, but the XRD pattern of BMO80 after the cyclic experiment in pure water (marked as BMO80-After) shows shift of (020) and (131) peaks to the high 2θ, suggesting decrease of interplanar spacings, with the (111) peak position remaining unvaried (Fig. S16), which likely arises from the loss of Br from the crystal lattice, according to the proposed structure of BMO80 (Fig. 1c–g).

XPS was performed to confirm structures of the samples. As shown in Fig. 9a and b, BMO80-After-M exhibits similar Bi 4 f and Br 3d peaks as BMO80, manifesting their similar structures, however, the Bi–O, Bi^{2+}, Bi–OH, and Br^- peaks of BMO80-After show 0.2, 0.1, 0.2, and 0.3 eV shift to the low binding energy, respectively, relative to those of BMO80, revealing the remarkable structural change of BMO80-After. Based on

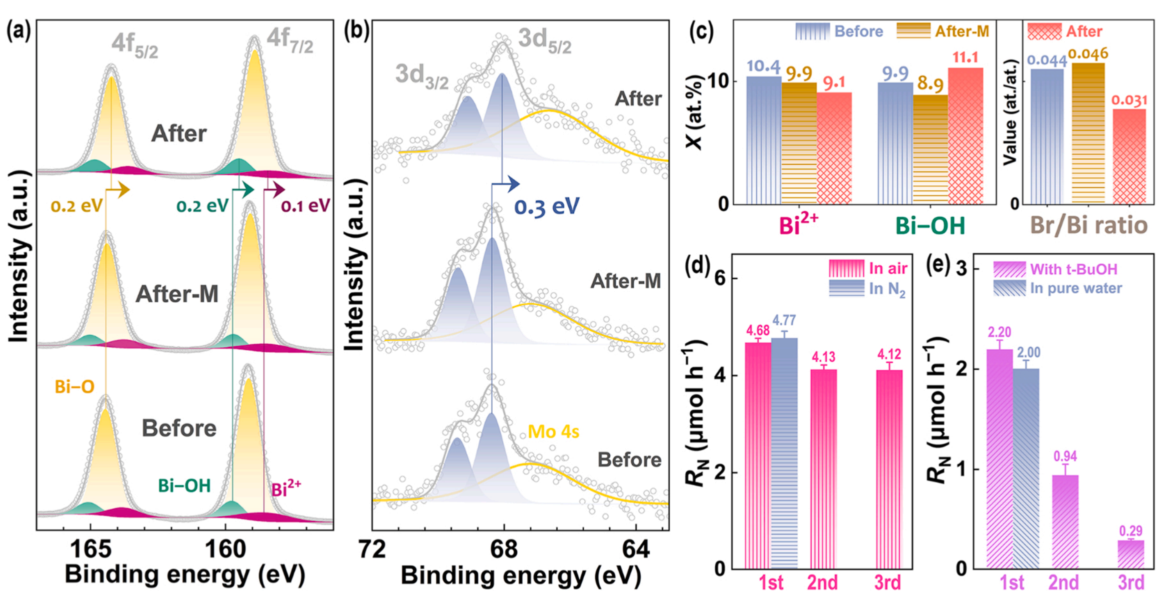

Fig. 9. (a) Bi 4 f and (b) Br 3d core-level XPS spectra of BMO80, BMO80 after the cyclic experiment in pure water (BMO80-After), and BMO80 after the cyclic experiment in methanol solution (BMO80-After-M); (c) molar content (X) of Bi species calculated according to the XPS data; (d) three-consecutive runs for photocatalytic N_2 reduction on BMO80 in the methanol solution and in the air, with the data in N_2 atmosphere for comparison; and (e) three-consecutive runs of photocatalytic N_2 reduction on BMO80 in t-butyl alcohol (t-BuOH) aqueous water, with the data in pure water for comparison.

the XPS data (Table S3), the $X(Bi^{2+})$ and X(Bi−OH) of BMO80-After-M are only slightly lower than those of BMO80 and their Br/Bi molar ratios are similar (~0.045), further demonstrating the structural stability of BMO80-After-M (Fig. 9c), however, BMO80-After exhibits remarkably smaller $X(Bi^{2+})$, greater X(Bi−OH), and a considerably smaller Br/Bi molar ratio (0.031) than BMO80, indicative of the loss of Br, which may be replaced by −OH, accompanied with reduction of Ov, consistent with the XRD results. These variations might be caused by oxidation of holes (Fig. S17).

To confirm the role of holes, the photocatalytic nitrogen reduction on BMO80 in the methanol solution was carried out in air. As shown in Fig. 9d, BMO80 exhibits similar photoactivity as in the N_2 atmosphere, and its photoactivity nearly remains constant after three-consecutive runs, suggesting the generated O_2 by hole oxidation.

of H_2O is not responsible for the structural damage of BMO80-After. The photocatalytic N_2 reduction on BMO80 was also performed in the t-butyl alcohol (a quencher of hydroxyl radicals [55]) aqueous solution and the t-butyl alcohol did not enhance the photochemical stability of BMO80 (Fig. 9e), indicating hydroxyl radicals are not the key factor leading to structural damage of BMO80-After·H_2O_2 processed BMO80 exhibits remarkable decrease of photocatalytic N_2 reduction activity in pure water (Fig. S18), indicating H_2O_2 is a detrimental factor to stability of BMO80-After, however, H_2O_2 was not detected by colorimetry in the photocatalytic process of BMO80 in pure water (Fig. S19), suggesting the structure of BMO80-After was not damaged by H_2O_2. Therefore, it is likely the direct oxidation of holes that leads to loss of Br with substitution of OH and reduction of Ov in BMO80-After (Fig. S17). To further confirm the reduction of Ov in BMO80-After caused by oxidation of holes, the cyclic experiment of photocatalytic N_2 reduction on BMO was also conducted in pure water. As shown in Fig. S20, the production rates of NH_3 on BMO remarkably decrease after the cyclic experiment, probably suggesting the reduction of Ov because of oxidation of holes. On the whole, more stable Br doping and Ov structures in Bi_2MoO_6 need be explored in future from the perspective of practical application.

To unravel the photocatalytic nitrogen fixation mechanism on BMO80, in-situ FT-IR spectroscopy was performed. Fig. 10a shows FT-IR spectra of BMO80 with adsorption of N_2 in the dark for up to 80 min, where absorption bands I (~3610 cm^{-1}), II (~3380 cm^{-1}), III (~3050 cm^{-1}), V (~1668 cm^{-1}), and VI (~1547 cm^{-1}) are ascribed to the N − H stretching vibration, the stretching vibration of adsorbed hydroxyl species, the NH_4^+ stretching vibration, chemisorbed N_2, and adsorbed NH_3, respectively [56]. The intensity of these absorption bands gradually increases with adsorption time. Under light irradiation, the spectrum changes rapidly and shows considerably enhanced absorption bands (Fig. S21), indicating instantaneously enhanced N_2 adsorption and conversion of N_2 to NH_3. The absorption band positions vary prominently relative to those in the dark (Fig. 10b), likely influenced by the photogenerated charge. Absorption bands i (~3390 cm^{-1}) and ii (~3230 cm^{-1}) are attributed to N − H and surface O−H stretching vibrations, respectively. The absorption bands iv (~1650 cm^{-1}) and vi (~1480 cm^{-1}) can be ascribed to the N − H bending vibration, and the absorption band iii (~2882 cm^{-1}), v (~1600 cm^{-1}), vii (~1330 cm^{-1}), and viii (~1070 cm^{-1}) are assigned to NH_4^+, chemisorbed N_2, adsorbed NH_3, and the N − N stretching vibration, respectively [30,57,58]. It should be noted that the N_2 molecules exhibit no IR absorption unless the N≡N triple bonds are broken through formation of Ov−N≡N [30]. Therefore, the gradual increase of absorption band intensity of N-related species with light illumination time (Fig. 10c) indicates N_2 molecules can easily adsorb at the Ov and the N≡N triple bonds can be continuously activated to finally form NH_3 or NH_4^+.

Fig. 10d compares the FT-IR spectra acquired after 100-min light illumination and rested in the dark and N_2 atmosphere for different time. After the light was turned off, relative shift of absorption bands V (~1643 cm^{-1}, assigned to chemisorbed N_2) and VI (~1412 cm^{-1},

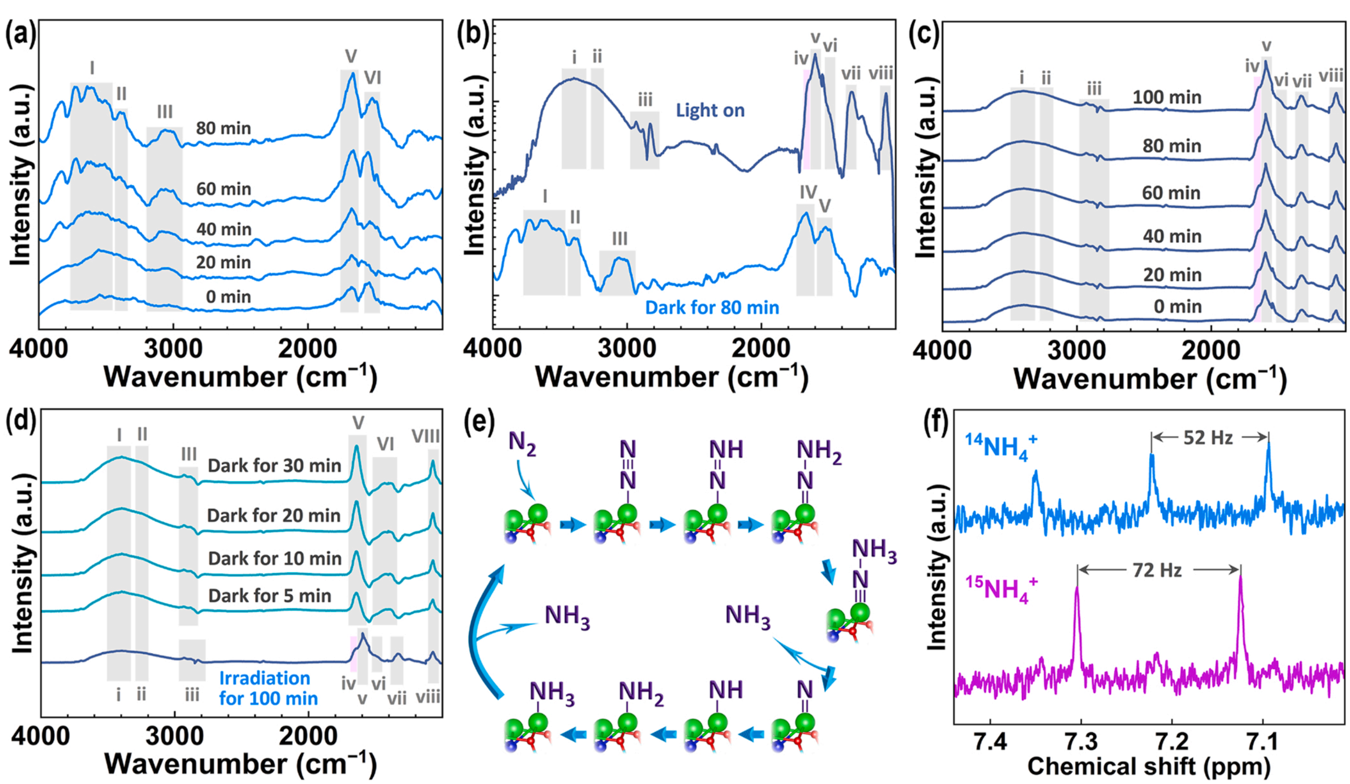

Fig. 10. In-situ FT-IR spectra of BMO80 (a) after adsorption of N_2 in the dark for up to 80 min, (b) after adsorption in the dark for 80 min and then light illumination started, (c) under light illumination for up to 100 min, and (d) after light illumination for 100 min and rested in the dark (in N_2) for up to 30 min; (e) schematic illustration for the N_2 activation and reduction at surface Bi^{2+} of BMO80 in line with the associative distal pathway; and (f) ^1H NMR spectra for $^{14}NH_4^+$ and $^{15}NH_4^+$ formed via photocatalytic $^{14}N_2$ and $^{15}N_2$ reduction on BMO80, respectively.

assigned to adsorbed NH_3) further demonstrates the influence of photoexcited charge. Apparently, absorption bands I (~3390 cm^{-1}, ascribed to the N – H stretching vibration), III (~2882 cm^{-1}, assigned to NH_4^+), V, and VIII (~1070 cm^{-1}, ascribed to the N – N stretching vibration) gradually increase with time, further manifesting the ready adsorption and activation of N_2 at the surface Ov of BMO80. According to reported similar results [56,59] and the fact that there is no N_2H_4 detected in the photocatalytic process (Fig. S22), the reduction of N_2 to NH_3 on BMO80 probably follows the associative distal pathway [60] (Fig. 10e). To corroborate the origin of NH_3 generated from N_2 reduction, the isotopic labeling research by using $^{15}N_2$ as the purging gas was conducted [61]. As shown in the ^1H NMR spectra (Fig. 10f), the isotopic labeled sample exhibited doublets of $^{15}NH_4^+$, distinctly different from the unlabeled sample exhibiting triplets of $^{14}NH_4^+$, which demonstrates that the generated NH_3 indeed originates from N_2 reduction.

4. Conclusions

Surface-layer Br doped and oxygen vacancy (Ov) modified Bi_2MoO_6 (BMO-Br-Ov) microspheres were solvothermally synthesized in ethylene glycol and generation of the enriched surface Ov in BMO-Br-Ov benefits from the Br doping by replacing MoO_4^{2-} with necessary OH cooridination. Compared with the bulk Bi_2MoO_6 (BMO), BMO-Br-Ov exhibits enhanced chemisorption of N_2 molecules, enlarged surface area, increased photogenerated charge separation and transfer efficiencies, and thus enhanced photocatalytic N_2 nitrogen activity. In pure water, the NH_3 production rate of BMO-Br-Ov is ~2.5 times that of BMO and 23 times that of Bi_2MoO_6 synthesized in water. The enhancement of N_2 chemisorption results from the new formed surface Ov and the fast charge separation arises from the introduction of a defect (Ov) level, close to the conduction band, in the bandgap and the surface-layer Br doping and Ov induced fabrication of the surface/inside homojunciton in BMO-Br-Ov. The photocatalytic reduction of N_2 to NH_3 on BMO-Br-Ov follows the associative distal pathway. BMO-Br-Ov exhibits lower photochemical stability in pure water owing to the hole oxidation induced Br loss and Ov reduction, but high stability in the methanol (eliminating holes) aqueous solution. This work provides a novel way to create rich surface Ov in Bi_2MoO_6 for efficient photocatalytic nitrogen fixation.

CRediT authorship contribution statement

Guoan Wang: Conceptualization, Methodology, Formal analysis, Writing – original draft. **Tingting Huo:** Methodology, Investigation, Formal analysis, Validation. **Quanhua Deng:** Methodology, Investigation, Formal analysis. **Fei Yu:** Methodology, Investigation, Formal analysis. **Yuguo Xia:** Methodology, Formal analysis. **Haiping Li:** Conceptualization, Writing – review & editing, Funding acquisition. **Wanguo Hou:** Funding acquisition, Writing – review & editing.

Declaration of Competing Interest

The authors declare that they have no known competing financial interests or personal relationships that could have appeared to influence the work reported in this paper.

Acknowledgements

This work was supported by the National Natural Science Foundation of China (No. 21872082) and the Young Scholars Program of Shandong University in China (No. 2018WLJH39). We also thank the assistance of Shandong University Structural Constituent and Physical Property Research Facilities (SDU SCPPRF) and Shiyanjia Lab (www. shiyanjia. com).

Appendix A. Supporting information

Supplementary data associated with this article can be found in the online version at doi:10.1016/j.apcatb.2022.121319.

References

[1] C.J.M. van der Ham, M.T.M. Koper, D.G.H. Hetterscheid, Challenges in reduction of dinitrogen by proton and electron transfer, Chem. Soc. Rev. 43 (2014) 5183–5191, https://doi.org/10.1039/C4CS00085D.
[2] Y. Huang, N. Zhang, Z. Wu, X. Xie, Artificial nitrogen fixation over bismuth-based photocatalysts: fundamentals and future perspectives, J. Mater. Chem. A 8 (2020) 4978–4995, https://doi.org/10.1039/C9TA13589H.
[3] T. Kandemir, M.E. Schuster, A. Senyshyn, M. Behrens, R. Schlögl, The Haber–Bosch process revisited: on the real structure and stability of "ammonia iron" under working conditions, Angew. Chem. Int. Ed. 52 (2013) 12723–12726, https://doi.org/10.1002/anie.201305812.
[4] V. Smil, Enriching the earth: Fritz Haber. Carl Bosch, and the transformation of world food production, MIT Press, 2001.
[5] H. Hirakawa, M. Hashimoto, Y. Shiraishi, T. Hirai, Photocatalytic conversion of nitrogen to ammonia with water on surface oxygen vacancies of titanium dioxide, J. Am. Chem. Soc. 139 (2017) 10929–10936, https://doi.org/10.1021/jacs.7b06634.
[6] S. Wang, F. Ichihara, H. Pang, H. Chen, J. Ye, Nitrogen fixation reaction derived from nanostructured catalytic materials, Adv. Funct. Mater. 28 (2018), 1803309, https://doi.org/10.1002/adfm.201803309.
[7] X. Gao, Y. Shang, L. Liu, F. Fu, Chemisorption-enhanced photocatalytic nitrogen fixation via 2D ultrathin p-n heterojunction AgCl/δ-Bi_2O_3 nanosheets, J. Catal. 371 (2019) 71–80, https://doi.org/10.1016/j.jcat.2019.01.002.
[8] W. He, Y. Sun, G. Jiang, Y. Li, X. Zhang, Y. Zhang, Y. Zhou, F. Dong, Defective Bi_4MoO_9/Bi metal core/shell heterostructure: enhanced visible light photocatalysis and reaction mechanism, Appl. Catal. B 239 (2018) 619–627, https://doi.org/10.1016/j.apcatb.2018.08.064.
[9] X. Meng, Z. Zhang, Bismuth-based photocatalytic semiconductors: introduction, challenges and possible approaches, J. Mol. Catal. A 423 (2016) 533–549, https://doi.org/10.1016/j.molcata.2016.07.030.
[10] R. Shi, Y. Zhao, G.I. Waterhouse, S. Zhang, T. Zhang, Defect engineering in photocatalytic nitrogen fixation, ACS Catal. 9 (2019) 9739–9750, https://doi.org/10.1021/acscatal.9b03246.
[11] Q. Meng, C. Lv, J. Sun, W. Hong, W. Xing, L. Qiang, G. Chen, X. Jin, High-efficiency Fe-mediated Bi_2MoO_6 nitrogen-fixing photocatalyst: reduced surface work function and ameliorated surface reaction, Appl. Catal. B 256 (2019), 117781, https://doi.org/10.1016/j.apcatb.2019.117781.
[12] C. Shi, X. Dong, Y. Hao, X. Wang, H. Ma, X. Zhang, The controllable fabrication of a novel hierarchical nanosheet-assembled Bi_2MoO_6 hollow micronbox with ultra-high surface area for excellent solar to chemical energy conversion, RSC Adv. 7 (2017) 50040–50043, https://doi.org/10.1039/C7RA10060D.
[13] E. Vesali-Kermani, A. Habibi-Yangjeh, H. Diarmand-Khalilabad, S. Ghosh, Nitrogen photofixation ability of g-C_3N_4 nanosheets/Bi_2MoO_6 heterojunction photocatalyst under visible-light illumination, J. Colloid Interface Sci. 563 (2020) 81–91, https://doi.org/10.1016/j.jcis.2019.12.057.
[14] X. Xue, R. Chen, C. Yan, Y. Hu, W. Zhang, S. Yang, L. Ma, G. Zhu, Z. Jin, Efficient photocatalytic nitrogen fixation under ambient conditions enabled by the heterojunctions of n-type Bi_2MoO_6 and oxygen-vacancy-rich p-type BiOBr, Nanoscale 11 (2019) 10439–10445, https://doi.org/10.1039/C9NR02279A.
[15] M. Lan, N. Zheng, X. Dong, X. Ren, J. Wu, H. Ma, X. Zhang, Facile construction of a hierarchical Bi@BiOBr-Bi_2MoO_6 ternary heterojunction with abundant oxygen vacancies for excellent photocatalytic nitrogen fixation, Sustain. Energy Fuels 5 (2021) 2927–2933, https://doi.org/10.1039/D1SE00178G.
[16] W. Liu, K. Yin, K. Yuan, S. Zuo, S. Yang, C. Yao, M. Chen, In situ synthesis of Bi_2MoO_6@C@attapulgite photocatalyst for enhanced photocatalytic nitrogen fixation ability under simulated solar irradiation, Colloid Surf. A 591 (2020), 124488, https://doi.org/10.1016/j.colsurfa.2020.124488.
[17] Y. Hao, X. Dong, S. Zhai, H. Ma, X. Wang, X. Zhang, Hydrogenated bismuth molybdate nanoframe for efficient sunlight-driven nitrogen fixation from air, Chem. Eur. J. 22 (2016) 18722–18728, https://doi.org/10.1002/chem.201604510.
[18] G. Li, W. Yang, S. Gao, Q. Shen, J. Xue, K. Chen, Q. Li, Creation of rich oxygen vacancies in bismuth molybdate nanosheets to boost the photocatalytic nitrogen fixation performance under visible light illumination, Chem. Eng. J. 404 (2021), 127115, https://doi.org/10.1016/j.cej.2020.127115.
[19] L. Yang, J. Guo, J. Zhang, S. Zhang, W. Dai, X. Xiao, X. Luo, S. Luo, Utter degradation of toluene with inhibiting the generation of benzene by self-supporting Bi_2MoO_6 nanoflakes featuring Ov-enriched interface, Chem. Eng. J. 427 (2022), 131550, https://doi.org/10.1016/j.cej.2021.131550.
[20] Z. Sun, X. Yang, X.-F. Yu, L. Xia, Y. Peng, Z. Li, Y. Zhang, J. Cheng, K. Zhang, J. Yu, Surface oxygen vacancies of Pd/Bi_2MoO_{6-x} acts as "Electron Bridge" to promote photocatalytic selective oxidation of alcohol, Appl. Catal. B 285 (2021), 119790, https://doi.org/10.1016/j.apcatb.2020.119790.
[21] X. Yang, S. Wang, N. Yang, W. Zhou, P. Wang, K. Jiang, S. Li, H. Song, X. Ding, H. Chen, J. Ye, Oxygen vacancies induced special CO_2 adsorption modes on Bi_2MoO_6 for highly selective conversion to CH_4, Appl. Catal. B 259 (2019), 118088, https://doi.org/10.1016/j.apcatb.2019.118088.

[22] S. Wang, X. Ding, N. Yang, G. Zhan, X. Zhang, G. Dong, L. Zhang, H. Chen, Insight into the effect of bromine on facet-dependent surface oxygen vacancies construction and stabilization of Bi_2MoO_6 for efficient photocatalytic NO removal, Appl. Catal. B 265 (2020), 118585, https://doi.org/10.1016/j.apcatb.2019.118585.
[23] N. Zhang, A. Jalil, D. Wu, S. Chen, Y. Liu, C. Gao, W. Ye, Z. Qi, H. Ju, C. Wang, Refining defect states in $W_{18}O_{49}$ by Mo doping: a strategy for tuning N_2 activation towards solar-driven nitrogen fixation, J. Am. Chem. Soc. 140 (2018) 9434–9443, https://doi.org/10.1021/jacs.8b02076.
[24] H. Wang, S. Jiang, S. Chen, X. Zhang, W. Shao, X. Sun, Z. Zhao, Q. Zhang, Y. Luo, Y. Xie, Insights into the excitonic processes in polymeric photocatalysts, Chem. Sci. 8 (2017) 4087–4092, https://doi.org/10.1039/c7sc00307b.
[25] N.K. Veldurthi, N.K. Eswar, S.A. Singh, G. Madras, Heterojunction $ZnWO_4$/$ZnFe_2O_4$ composites with concerted effects and integrated properties for enhanced photocatalytic hydrogen evolution, Catal. Sci. Technol. 8 (2018) 1083–1093, https://doi.org/10.1039/C7CY02281F.
[26] J.P. Perdew, K. Burke, M. Ernzerhof, Generalized gradient approximation made simple, Phys. Rev. Lett. 77 (1996) 3865–3868, https://doi.org/10.1103/PhysRevLett.77.3865.
[27] G. Kresse, D. Joubert, From ultrasoft pseudopotentials to the projector augmented-wave method, Phys. Rev. B 59 (1999) 1758–1775, https://doi.org/10.1103/PhysRevB.59.1758.
[28] G. Kresse, J. Furthmüller, Efficiency of ab-initio total energy calculations for metals and semiconductors using a plane-wave basis set, Comp. Mater. Sci. 6 (1996) 15–50, https://doi.org/10.1016/0927-0256(96)00008-0.
[29] G. Kresse, J. Furthmüller, Efficient iterative schemes for ab initio total-energy calculations using a plane-wave basis set, Phys. Rev. B 54 (1996) 11169–11186, https://doi.org/10.1103/PhysRevB.54.11169.
[30] S. Wang, X. Hai, X. Ding, K. Chang, Y. Xiang, X. Meng, Z. Yang, H. Chen, J. Ye, Light-switchable oxygen vacancies in ultrafine Bi_5O_7Br nanotubes for boosting solar-driven nitrogen fixation in pure water, Adv. Mater. 29 (2017), 1701774, https://doi.org/10.1002/adma.201701774.
[31] K. Jing, W. Ma, Y. Ren, J. Xiong, B. Guo, Y. Song, S. Liang, L. Wu, Hierarchical Bi_2MoO_6 spheres in situ assembled by monolayer nanosheets toward photocatalytic selective oxidation of benzyl alcohol, Appl. Catal. B 243 (2019) 10–18, https://doi.org/10.1016/j.apcatb.2018.10.027.
[32] Y. Huang, Y. Zhu, S. Chen, X. Xie, Z. Wu, N. Zhang, Schottky junctions with Bi cocatalyst for taming aqueous phase N_2 reduction toward enhanced solar ammonia production, Adv. Sci. 8 (2021), 2003626, https://doi.org/10.1002/advs.202003626.
[33] M.K. Kavitha, K.B. Jinesh, R. Philip, P. Gopinath, H. John, Defect engineering in ZnO nanocones for visible photoconductivity and nonlinear absorption, Phys. Chem. Chem. Phys. 16 (2014) 25093–25100, https://doi.org/10.1039/C4CP03847A.
[34] W. Phasayavan, M. Japa, S. Pornsuwan, D. Tantraviwat, F. Kielar, V.B. Golovko, S. Jungsuttiwong, B. Inceesungvorn, Oxygen-deficient bismuth molybdate nanocatalysts: synergistic effects in boosting photocatalytic oxidative coupling of benzylamine and mechanistic insight, J. Colloid Interface Sci. 581 (2021) 719–728, https://doi.org/10.1016/j.jcis.2020.07.140.
[35] X. Xie, Q.-U. Hassan, H. Lu, F. Rao, J. Gao, G. Zhu, In situ construction of oxygen-vacancy-rich Bi^0@$Bi_2WO_{6\text{-}x}$ microspheres with enhanced visible light photocatalytic for NO removal, Chin. Chem. Lett. 32 (2021) 2038–2042, https://doi.org/10.1016/j.cclet.2020.10.002.
[36] K. Zhang, G. Zhang, J. Qu, H. Liu, Disordering the atomic structure of Co(II) oxide via B-doping: an efficient oxygen vacancy introduction approach for high oxygen evolution reaction electrocatalysts, Small 14 (2018), 1802760, https://doi.org/10.1002/smll.201802760.
[37] J. Meng, Q. Lin, T. Chen, X. Wei, J. Li, Z. Zhang, Oxygen vacancy regulation on tungsten oxides with specific exposed facets for enhanced visible-light-driven photocatalytic oxidation, Nanoscale 10 (2018) 2908–2915, https://doi.org/10.1039/C7NR08590G.
[38] G. Ba, T. Huo, Q. Deng, H. Li, W. Hou, Mechanochemical synthesis of nitrogen-deficient mesopore-rich polymeric carbon nitride with highly enhanced photocatalytic performance, ACS Sustain. Chem. Eng. 8 (2020) 18606–18615, https://doi.org/10.1021/acssuschemeng.0c06851.
[39] B. Lei, W. Cui, J. Sheng, H. Wang, P. Chen, J. Li, Y. Sun, F. Dong, Synergistic effects of crystal structure and oxygen vacancy on Bi_2O_3 polymorphs: intermediates activation, photocatalytic reaction efficiency, and conversion pathway, Sci. Bull. 65 (2020) 467–476, https://doi.org/10.1016/j.scib.2020.01.007.
[40] K. Jing, J. Xiong, N. Qin, Y. Song, L. Li, Y. Yu, S. Liang, L. Wu, Development and photocatalytic mechanism of monolayer Bi_2MoO_6 nanosheets for the selective oxidation of benzylic alcohols, Chem. Commun. 53 (2017) 8604–8607, https://doi.org/10.1039/C7CC04052K.
[41] X. Zeng, Z. Xu, X. Gong, Y. Wan, Facile synthesis of Zn-doped $Bi(OH)_3$ with upward surface band bending and its enhanced visible light photocatalytic activity, Desalin. Water Treat. 177 (2020) 186–196, https://doi.org/10.5004/dwt.2020.24910.
[42] H. Bai, W. Yi, J. Li, G. Xi, Y. Li, H. Yang, J. Liu, Direct growth of defect-rich MoO_{3-x} ultrathin nanobelts for efficiently catalyzed conversion of isopropyl alcohol to propylene under visible light, J. Mater. Chem. A 4 (2016) 1566–1571, https://doi.org/10.1039/C5TA08603E.
[43] Y. Peng, J. Xu, T. Liu, Y.-g Mao, Controlled synthesis of one-dimensional BiOBr with exposed (110) facets and enhanced photocatalytic activity, CrystEngComm 19 (2017) 6473–6480, https://doi.org/10.1039/C7CE01452J.
[44] A. Maleki, J. Rahimi, Z. Hajizadeh, M. Niksefat, Synthesis and characterization of an acidic nanostructure based on magnetic polyvinyl alcohol as an efficient heterogeneous nanocatalyst for the synthesis of α-aminonitriles, J. Organomet. Chem. 881 (2019) 58–65, https://doi.org/10.1016/j.jorganchem.2018.12.002.
[45] Z. Wang, W. Wang, L. Zhang, D. Jiang, Surface oxygen vacancies on Co_3O_4 mediated catalytic formaldehyde oxidation at room temperature, Catal. Sci. Technol. 6 (2016) 3845–3853, https://doi.org/10.1039/C5CY01709B.
[46] K. Sivaranjani, C.S. Gopinath, Porosity driven photocatalytic activity of wormhole mesoporous $TiO_{2\text{-}x}N_x$ in direct sunlight, J. Mater. Chem. 21 (2011) 2639–2647, https://doi.org/10.1039/C0JM03825C.
[47] S. Sun, G. Shen, Z. Chen, L. Pan, X. Zhang, J.-J. Zou, Harvesting urbach tail energy of ultrathin amorphous nickel oxide for solar-driven overall water splitting up to 680 nm, Appl. Catal. B 285 (2021), 119798, https://doi.org/10.1016/j.apcatb.2020.119798.
[48] W. Wang, W. Zhao, H. Huang, R. Chen, H. Shi, A 2D/2D S-scheme photo-Fenton catalyst based on ultrathin Bi_2MoO_6 and Fe_2O_3 hexagonal nanosheets for efficient tetracycline degradation, Catal. Sci. Technol. 11 (2021) 2948–2956, https://doi.org/10.1039/D1CY00051A.
[49] R. Schafranek, S. Payan, M. Maglione, A. Klein, Barrier height at (Ba, Sr)TiO_3/Pt interfaces studied by photoemission, Phys. Rev. B 77 (2008), 195310, https://doi.org/10.1103/PhysRevB.77.195310.
[50] S. Sharma, S. Ghosh, T. Ahmed, S. Ray, S. Islam, U. Salzner, A. Ghosh, S. Seki, S. Patil, Fermi level pinning induced by doping in air stable n-type organic semiconductor, ACS Appl. Electron. Mater. 2 (2020) 66–73, https://doi.org/10.1021/acsaelm.9b00742.
[51] Y. Zhao, Y. Zhao, R. Shi, B. Wang, G.I.N. Waterhouse, L.-Z. Wu, C.-H. Tung, T. Zhang, Tuning oxygen vacancies in ultrathin TiO_2 nanosheets to boost photocatalytic nitrogen fixation up to 700 nm, Adv. Mater. 31 (2019), 1806482, https://doi.org/10.1002/adma.201806482.
[52] Z. Liang, X. Zhuang, Z. Tang, H. Li, L. Liu, W. Kang, Soft-template induced synthesis of high-crystalline polymeric carbon nitride with boosted photocatalytic performance, J. Mater. Chem. A 9 (2021) 6805–6810, https://doi.org/10.1039/d1ta00342a.
[53] T. Huo, G. Ba, Q. Deng, F. Yu, G. Wang, H. Li, W. Hou, A dual strategy for synthesizing carbon/defect comodified polymeric carbon nitride porous nanotubes with boosted photocatalytic hydrogen evolution and synchronous contaminant degradation, Appl. Catal. B 287 (2021), 119995, https://doi.org/10.1016/j.apcatb.2021.119995.
[54] M. Xu, W. Wang, Y. Zhong, X. Xu, J. Wang, W. Zhou, Z. Shao, Enhancing the triiodide reduction activity of a perovskite-based electrocatalyst for dye-sensitized solar cells through exsolved silver nanoparticles, J. Mater. Chem. A 7 (2019) 17489–17497, https://doi.org/10.1039/C9TA05005A.
[55] H. Li, J. Liu, W. Hou, N. Du, R. Zhang, X. Tao, Synthesis and characterization of g-C_3N_4/Bi_2MoO_6 heterojunctions with enhanced visible light photocatalytic activity, Appl. Catal. B 160 (161) (2014) 89–97, https://doi.org/10.1016/j.apcatb.2014.05.0l9.
[56] P. Li, Z. Zhou, Q. Wang, M. Guo, S. Chen, J. Low, R. Long, W. Liu, P. Ding, Y. Wu, Visible-light-driven nitrogen fixation catalyzed by Bi_5O_7Br nanostructures: enhanced performance by oxygen vacancies, J. Am. Chem. Soc. 142 (2020) 12430–12439, https://doi.org/10.1021/jacs.0c05097.
[57] H. Li, J. Shang, Z. Ai, L. Zhang, Efficient visible light nitrogen fixation with BiOBr nanosheets of oxygen vacancies on the exposed {001} facets, J. Am. Chem. Soc. 137 (2015) 6393–6399, https://doi.org/10.1021/jacs.5b03105.
[58] R. Hao, W. Sun, Q. Liu, X. Liu, J. Chen, X. Lv, W. Li, Y.-p Liu, Z. Shen, Efficient electrochemical nitrogen fixation over isolated Pt sites, Small 16 (2020), 2000015, https://doi.org/10.1002/smll.202000015.
[59] X. Xue, R. Chen, H. Chen, Y. Hu, Q. Ding, Z. Liu, L. Ma, G. Zhu, W. Zhang, Q. Yu, Oxygen vacancy engineering promoted photocatalytic ammonia synthesis on ultrathin two-dimensional bismuth oxybromide nanosheets, Nano Lett. 18 (2018) 7372–7377, https://doi.org/10.1021/acs.nanolett.8b03655.
[60] G. Zhang, Y. Li, C. He, X. Ren, P. Zhang, H. Mi, Recent progress in 2D catalysts for photocatalytic and electrocatalytic artificial nitrogen reduction to ammonia, Adv. Energy Mater. 11 (2021), 2003294, https://doi.org/10.1002/aenm.202003294.
[61] T. Hou, Y. Xiao, P. Cui, Y. Huang, X. Tan, X. Zheng, Y. Zou, C. Liu, W. Zhu, S. Liang, L. Wang, Operando oxygen vacancies for enhanced activity and stability toward nitrogen photofixation, Adv. Energy Mater. 9 (2019), 1902319, https://doi.org/10.1002/aenm.201902319.